Astronomy & Astrophysics manuscript no. rxs42
November 21, 2019
©ESO 2019

arXiv:1911.08904v1 [astro-ph.HE] 19 Nov 2019

New mysteries and challenges from the Toothbrush relic: wideband observations from 550 MHz to 8 GHz

K. Rajpurohit[1,2], M. Hoeft[3], F. Vazza[1,2,4], L. Rudnick[5], R. J. van Weeren[6], D. Wittor[1,2,4], A. Drabent[3] M. Brienza[1,2], F. Loi[1], E. Bonnassieux[1], N. Locatelli[1], R. Kale[7], and C. Dumba[8]

[1] Dipartimento di Fisica e Astronomia, Universitát di Bologna, via P. Gobetti 93/2, I-40129, Bologna, Italy
e-mail: kamlesh.rajpurohit@unibo.it
[2] INAF-Istituto di Radio Astronomia, Via Gobetti 101, Bologna, Italy
[3] Thüringer Landessternwarte (TLS), Sternwarte 5, 07778 Tautenburg, Germany
[4] Hamburger Sternwarte, Universität Hamburg, Gojenbergsweg 112, D-21029, Hamburg, Germany
[5] Minnesota Institute for Astrophysics, University of Minnesota, 116 Church St. S.E., Minneapolis, MN 55455, USA
[6] Leiden Observatory, Leiden University, P.O. Box 9513, NL-2300 RA Leiden, The Netherlands
[7] National Centre for Radio Astrophysics, Tata Institute of Fundamental Research, P. B. No. 3, Ganeshkhind, Pune 411007, India
[8] Mbarara University of Science and Technology, Mbarara, Uganda

November 21, 2019

ABSTRACT

Context. Radio relics are diffuse extended synchrotron sources that originate from shock fronts induced by galaxy cluster mergers. The actual particle acceleration mechanism at the shock fronts is still under debate. The galaxy cluster 1RXS J0603.3+4214 hosts one of the most intriguing examples of radio relics, known as the Toothbrush.

Aims. To understand the mechanism(s) that accelerate relativistic particles in the intracluster medium (ICM), we investigate the spectral properties of large scale diffuse extended sources in the merging galaxy cluster 1RXS J0603.3+4214.

Methods. We present new wideband radio continuum observations made with uGMRT and VLA. Our new observations in combination with previously published data, allowed us to carry out a detailed high spatial resolution spectral and curvature analysis of the known diffuse radio emission sources, over a broad range of frequencies.

Results. The integrated spectrum of the Toothbrush follows closely a power law over close to 2 decades in frequency, with a spectral index of -1.16 ± 0.02. We do not find any evidence of spectral steepening below 8 GHz. The subregions of the main Toothbrush also exhibit near-perfect power laws, implying a very regular combination of shock properties across the shock front. Recent numerical simulations show an intriguing similar spectral index, suggesting that the radio spectrum is dominated by the average over the inhomogeneities within the shock, with most of the emission coming from the tail of the Mach number distribution. In contrast to the Toothbrush, the spectrum of the fainter relics show a high frequency steepening. Moreover, also the integrated spectrum of the halo follows a power law from 150 MHz to 3 GHz with a spectral index of -1.16 ± 0.04. We do not find any evidence for spectral curvature, not even in subareas of the halo. This suggest a homogeneous acceleration throughout the cluster volume. Between the "brush" region of the Toothbrush and the halo, the color-color analysis revealed emission that was consistent with an overlap between the two different spectral regions.

Conclusions. None of the relic structures, the Toothbrush as a whole or its subregions or the other two fainter relics, show spectral shapes consistent with a single injection of relativistic electrons, such as at a shock, followed by synchrotron aging in a relatively homogeneous environment. Inhomogeneities in some combination of Mach number, magnetic field strengths and projection effects dominate the observed spectral shapes.

Key words. Galaxies: clusters: individual (1RXS J0603.3+4214) – Galaxies: clusters: intracluster medium – large-scale structures of universe – Acceleration of particles – Radiation mechanism: non-thermal: shock waves

1. Introduction

Radio observations of a fraction of galaxy clusters reveal the presence of spectacular large scale diffuse synchrotron sources. These diffuse sources are known as radio relics and radio halos (see van Weeren et al. 2019, for a recent review). They show a typical synchrotron spectrum[1]. In the hierarchical model of structure formation, galaxy clusters form through a sequence of mergers with smaller substructures. During cluster mergers, shock waves and turbulence are produced within the intracluster medium (ICM). Merger driven shocks and turbulence are expected to be efficient accelerators of cosmic rays (CRs) to relativistic energies and may amplify cluster's magnetic fields.

Radio halos are typically unpolarized sources located in the center of galaxy clusters and have an extent of ∼ Mpc. They roughly follow the X-ray emission from the ICM. The currently favored scenario for the formation of radio halos involves the re-acceleration of CR electrons (CRe) via magneto-hydrodynamical turbulence (e.g. Brunetti et al. 2001; Petrosian 2001; Brunetti & Jones 2014).

Radio relics are Mpc-sized elongated radio sources typically found in the periphery of merging galaxy clusters (see van Weeren et al. 2019, for a review). They are usually strongly polarized (Bonafede et al. 2009, 2012a; van Weeren et al. 2011,

[1] $S(\nu) \propto \nu^{\alpha}$ with spectral index α

Table 1. Observations overview

	VLA S-band		VLA C-band	uGMRT
	B-configuration	C-configuration	C-configuration	band 4
Observation date	September 9, 2017	November 29, 2018	November 18, 2018	September 14, 2018
Frequency range	2-4 GHz	2-4 GHz	4-8 GHz	550-750 MHz
Channel width	2 MHz	2 MHz	27 MHz	49 kHz
No of IF	16	16	36	1
No of channels per IF	64	64	64	4096
Integration time	3 s	5 s	2 s	8 s
On source time	3 hrs	5 hrs	5 hrs	8 hrs

Notes. Full Stokes polarization information was recorded for the VLA and the uGMRT observations.

2012; Kale et al. 2012; Owen et al. 2014). Relics are believed to originate from shock fronts induced by galaxy cluster mergers. This connection has been confirmed by sometimes finding shock fronts in the X-ray surface brightness distribution located where radio relics have been found (see e.g., Sarazin et al. 2013; Ogrean et al. 2013; Shimwell et al. 2015; van Weeren et al. 2016; Botteon et al. 2016; Thölken et al. 2018; Di Gennaro et al. 2019). The sizes of relics and their separations from the cluster center vary significantly, as well as their degree of association with shocks detected via X-ray observations, which makes it difficult to obtain a self-consistent theoretical model of their origin.

Relic emission is believed to be produced by diffusive shock acceleration (DSA) at the merger shocks (e.g. Bykov et al. 2019, for a recent review). Theoretical models predicting the observed radio power as a function of shock parameters have shown that the physical connection between shocks and radio emission is physically viable (e.g. Ensslin et al. 1998; Hoeft & Brüggen 2007; Kang et al. 2012). Numerical simulations have also been able to produce radio relics that reasonably resemble the observed ones in shape, total power and spectral index. (Hoeft et al. 2008; Battaglia et al. 2009; Skillman et al. 2011; Nuza et al. 2017).

However, several open problems arise when DSA is used to make quantitative predictions, pointing to limitations of the simplest models. There are three major difficulties: (1) the Mach numbers derived from X-ray observations are often significantly lower than those derived from radio observations; (2) DSA operating at shock fronts with Mach numbers $\mathcal{M} \leq 4$ requires an unrealistically high CRe acceleration efficiency in order to explain the relic luminosities (e.g. Vazza & Brüggen 2014; Vazza et al. 2015); (3) there is evidence that the spectral index of some relics shows steepening at higher frequencies (Stroe et al. 2016; Malu et al. 2016) or a flat integrated spectrum at low frequencies (Trasatti et al. 2015; Kierdorf et al. 2017), which is incompatible with the simplest models using DSA in a steady state.

An alternative mechanism is that mildly relativistic fossil electrons, perhaps from old radio galaxies, are reaccelerated in the shock (Kang & Ryu 2016). In this scenario, weaker shocks are able to accelerate the population of aged CRe. A volume filling population of fossil ($\geq 10^8$ yr) electrons which gets reaccelerated by shocks would alleviate the efficiency problem (e.g. Pinzke et al. 2013; Kang et al. 2012). This mechanism also predicts spectral steepening at high frequencies.

In the past decade, numerous studies have been dedicated to characterize the integrated spectra of relics (Itahana et al. 2015; Stroe et al. 2016; Kierdorf et al. 2017). The major question have been; Is there any steepening of the spectrum at high frequency? These studies have given different answers, owing to the differences in the covered frequency range, uv-coverage, and the type of observations (interferometric or single dish). The question of whether or not such a steepening exist is extremely important since it sheds light on the mechanisms which generate radio relics.

Recent high-resolution radio observations added new challenges as they unveiled the existence, within the relics, of filamentary structure on various scales (e.g. Owen et al. 2014; van Weeren et al. 2017b; Di Gennaro et al. 2018), including our first work on the "Toothbrush" relic (Rajpurohit et al. 2018). The origin of the filaments is unknown. Such features are found on scales that are still prohibitive to model even with modern numerical simulations of magnetic field growth in galaxy clusters (Donnert et al. 2018; Domínguez-Fernández et al. 2019). Therefore, gathering consistent radio data from them is presently crucial to understand their origin.

2. 1RXS J0603.3+4214

1RXS J0603.3+4214 is a merging galaxy cluster located at a redshift of $z = 0.22$. It hosts one of the largest and brightest relics, known as the Toothbrush (van Weeren et al. 2012). The cluster also contains two fainter relics (E and D) and a giant elongated radio halo.

The Toothbrush relic has long been an object of intense scrutiny. Numerous observational studies of the Toothbrush relic have been performed across many radio frequencies (van Weeren et al. 2012; Stroe et al. 2016; Kierdorf et al. 2017; van Weeren et al. 2016; Rajpurohit et al. 2018). It shows an unusual linear morphology with a size of about $\sim$ 1.9 Mpc and it extends far towards the cluster center, into the low density ICM. The relic structure shows three distinct components resembling the brush (B1) and the handle (B2+B3) of a toothbrush. The relic morphology is enigmatic. Brüggen et al. (2012) simulated a triple merger to explain how the structures created at the shock front could extend far into the low density ICM regime.

X-ray observations of 1RXS J0603.3+4214 revealed the presence of a weak shock of $\mathcal{M} \approx 1.5$ at the outer edge of the brush (Ogrean et al. 2013; van Weeren et al. 2016; Itahana et al. 2017). In contrast, the radio observations suggest a high Mach number shock of $\mathcal{M} \sim 3.7$ (Rajpurohit et al. 2018). There thus remains a large discrepancy between the Mach number derived from the X-ray and radio observations.

The Toothbrush has also been observed at high frequencies (> 2 GHz), where there is still some disagreement about its integrated radio spectral shape. Stroe et al. (2016) reported interferometric observations of the Toothbrush relic from 150 MHz to 30 GHz. They highlighted a steepening of the integrated spectrum beyond 2 GHz (from $\alpha = -1.00$ to -1.45). In contrast, the studies conducted with high frequency single dish observations at 4.8 GHz and 8.3 GHz have not shown significant evidence of spectral steepening (Kierdorf et al. 2017).

Table 2. Image properties

Band	Configuration	Name	Restoring Beam	Weighting	uv-cut	uv-taper	RMS noise μ Jy beam^{-1}
	C	IM1	$2\farcs7 \times 2\farcs6$	Briggs	none	none	3.2
VLA C-band	C	IM2	$5\farcs5 \times 5\farcs5$	Uniform	$\geq 0.4\,k\lambda$	$5''$	5.6
(4-8 GHz)	C	IM3	$8\farcs0 \times 8\farcs0$	Uniform	$\geq 0.4\,k\lambda$	$9''$	7.1
	BC	IM4	$2\farcs0 \times 1\farcs8$	Briggs	none	none	3.5
	BC	IM5	$5\farcs0 \times 5\farcs0$	Briggs	none	$6''$	4.8
	BC	IM6	$5\farcs5 \times 5\farcs5$	Uniform	$\geq 0.4\,k\lambda$	$6''$	5.6
VLA S-band	BC	IM7	$8\farcs0 \times 8\farcs0$	Uniform	$\geq 0.4\,k\lambda$	$9''$	6.4
(2-4 GHz)	BC	IM8	$10'' \times 10''$	Briggs	none	$11''$	7.8
	BC	IM9	$15'' \times 15''$	Briggs	none	$16''$	8.3
	BC	IM10	$15\farcs7 \times 15\farcs7$	Unifrom	$\geq 0.4\,k\lambda$	$16''$	9.1
	ABCD	IM11	$5\farcs5 \times 5\farcs5$	Uniform	$\geq 0.4\,k\lambda$	$6''$	7.1
VLA L-band†	ABCD	IM12	$8\farcs0 \times 8\farcs0$	Uniform	$\geq 0.4\,k\lambda$	$9''$	9.3
(1-2 GHz)	ABCD	IM13	$15\farcs7 \times 15\farcs7$	Uniform	$\geq 0.4\,k\lambda$	$16''$	16.2
	band 4	IM14	$5\farcs5 \times 4\farcs8$	Briggs	none	none	7.7
	band 4	IM15	$5\farcs5 \times 5\farcs5$	Uniform	$\geq 0.4\,k\lambda$	$5''$	16
uGMRT	band 4	IM16	$8\farcs0 \times 8\farcs0$	Uniform	$\geq 0.4\,k\lambda$	$8''$	18.2
(550-750 MHz)	band 4	IM17	$15'' \times 15''$	Briggs	none	$15''$	41.1
	band 4	IM18	$15\farcs7 \times 15\farcs7$	Uniform	$\geq 0.4\,k\lambda$	$15''$	55.6
	HBA	IM19	$5\farcs5 \times 5\farcs5$	Uniform	$\geq 0.4\,k\lambda$	none	141.0
LOFAR†	HBA	IM20	$8\farcs0 \times 8\farcs0$	Uniform	$\geq 0.4\,k\lambda$	$7''$	170.3
(120-180 MHz)	HBA	IM21	$15\farcs7 \times 15\farcs7$	Uniform	$\geq 0.4\,k\lambda$	$14''$	192.3

Notes. Imaging was always performed using multi-scale clean, `nterms`=2 and `wprojplanes`=500. For all images made with `Briggs` weighting we used `robust` = 0; † For data reduction steps, we refer to Rajpurohit et al. (2018) and van Weeren et al. (2016).

We studied the Toothbrush with the VLA in L-band (Rajpurohit et al. 2018). These observations allowed us to reveal filamentary structures on various scales, likely resulting from projection effects and the magnetic field distribution in the ICM. The Toothbrush is one of the brightest relics in the sky, thus, it provides an unparalleled chance to study these detailed structures.

Here, we present the results of further observations of the galaxy cluster 1RXS J0603.3+4214 with the Karl G. Jansky Very Large Array (VLA) and the upgraded Giant Metrewave Radio Telescope (uGMRT). These observations were mainly undertaken to provide higher-resolution radio emission from the Toothbrush relic, thus allowing us to study the exceptional radio emission in more detail than had been done previously.

The layout of this paper is as follows. In Sec. 3, we present an overview of the observations and data reduction. The new radio images are presented in Sec. 4. The results obtained with the spectral analysis are described in Sec. 5 and Sec. 6, followed by summary in Sec. 7.

Throughout this paper we assume a ΛCDM cosmology with $H_0 = 71$ km s^{-1} Mpc^{-1}, $\Omega_m = 0.3$, and $\Omega_\Lambda = 0.7$. At the cluster's redshift, $1''$ corresponds to a physical scale of 3.64 kpc. All output images are in the J2000 coordinate system and are corrected for primary beam attenuation.

3. Observations and Data Reduction

3.1. VLA observations

The galaxy cluster 1RXS J0603.3+4214 was observed with the VLA in C- and S-band (project code: 17B-367 and 18B-238). VLA C-band observations were taken in C-configuration while the S-band in B and C configurations. An overview of the observations and frequency bands is given in Table 1.

Due to the large angular size of the cluster, the C-band observation was pointed on the Toothbrush relic. The total recorded bandwidth was 4 GHz. The 34 spectral windows, each having 64 channels, were used to cover the frequency range of 4-8 GHz. S-band observations, pointed at the cluster center were split into 16 spectral windows, each divided into 64 channels to cover the frequency range of 2-4 GHz. The total recorded bandwidth for S-band observations were 2 GHz.

For both S- and C-band observations, all four polarization products (RR, RL, LR, and LL) were recorded. For each configuration, 3C147 and 3C138 were included as the primary calibrators, observed for 5-10 minutes each at the start of the observing run or in some case at the end of the observing run. J0555+3948 was included as a secondary calibrator and observed for $\sim$ 5 minutes after every 25-35 minutes target run.

The data were calibrated and imaged with `CASA` (McMullin et al. 2007) version 4.7.0. The data obtained from different observing runs were calibrated separately but in the same manner. The first step of data reduction consisted of the Hanning smoothing of the data. The data were then inspected for RFI (Radio Frequency Interference) and affected data were mitigated using `tfcrop` mode from `flagdata` task. The low amplitude RFI was flagged using `AOFlagger` (Offringa et al. 2010). Next, we determined and applied elevation dependent gain tables and antenna offsets positions. We then corrected for the bandpass using the calibrator 3C147. This prevents flagging of good data due to the bandpass roll-off at the edges of the spectral windows.

As a next step in the calibration, we used the S- and C-band 3C147 model provided by `CASA` software package and set the flux density scale according to Perley & Butler (2013). An initial phase calibration was performed using both the calibrators over a few channels per spectral window where the phase variations per channel were small. We corrected for parallel-hand delay and determined the bandpass response using the calibrator 3C147.

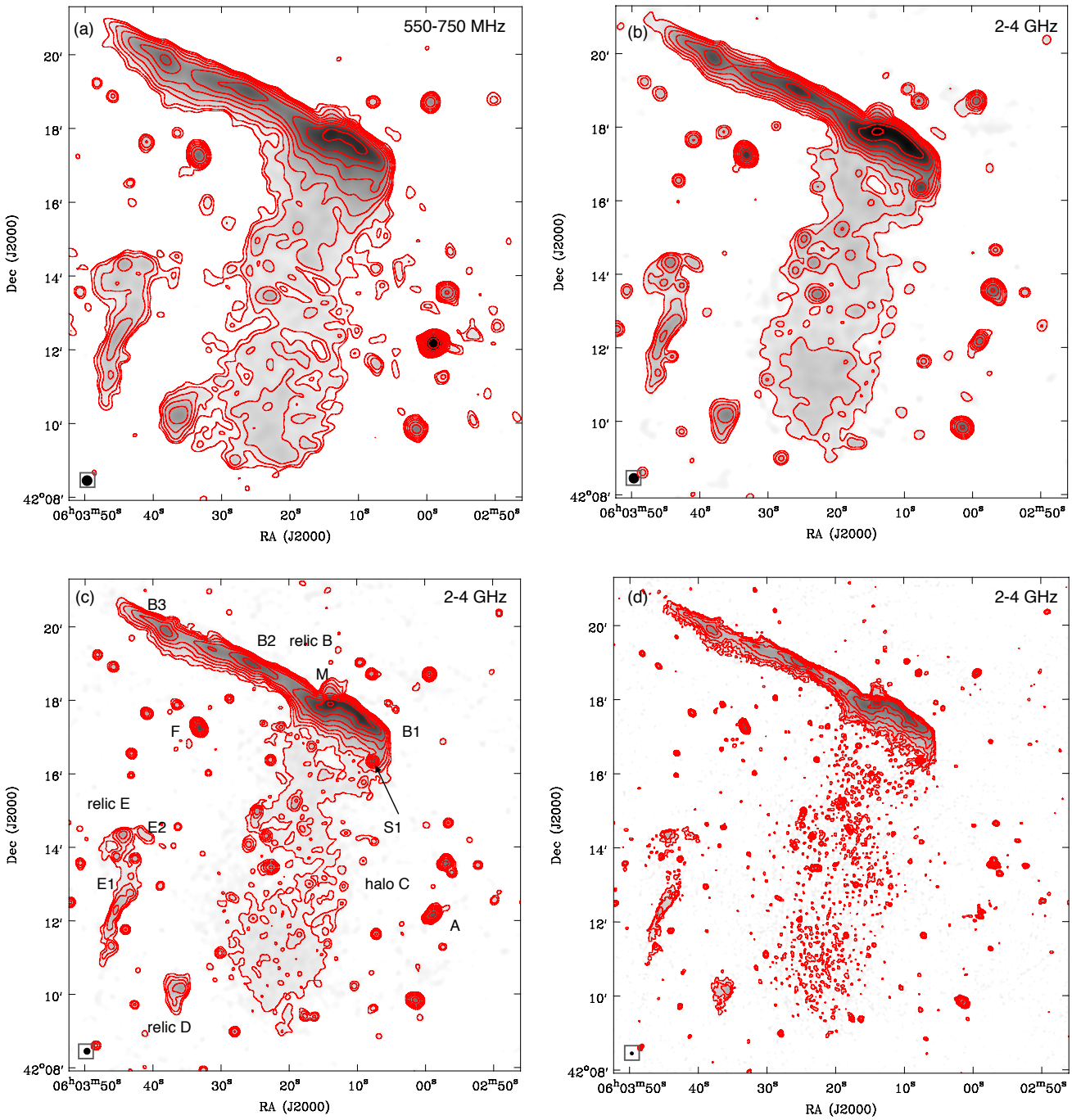


Fig. 1. uGMRT (550-750 MHz) and VLA S-band band images of 1RXS J0603.3+4214. The known diffuse emission sources, namely the bright Toothbrush, the other two fainter relics to the west and the large elongated halo are recovered in both the uGMRT and the VLA (S-band) observations. The image properties are given in Table 2. Here, panel (a), (b), (c), and (d) correspond to IM17, IM9, IM8, and IM5, respectively. Contour levels are drawn at $[1, 2, 4, 8, \dots] \times 4\,\sigma_{\rm rms}$. The beam size are indicated in the bottom left corner of the image.

Applying the bandpass and delay solutions, we proceeded with the gain calibration for the primary calibrators. The calibration solutions were then applied to the target field. For all different observing runs, the resulting calibrated data were averaged by a factor of 4 in frequency per spectral window.

After calibrating each configuration, we created initial images of the target field. The imaging of the data was executed with the `CASA` task `CLEAN`. For wide-field imaging, we employed the W-projection algorithm (Cornwell et al. 2008) which takes into consideration the effect of non-coplanarity. To take into account the spectral behavior of the bright sources in the field, we imaged each configuration using `nterms`=3 (Rau & Cornwell 2011). The deconvolution was always performed using a multi-scale multi frequency `CLEAN` algorithm (Rau & Cornwell 2011) and with `CLEAN` masks generated through `PyBDSF` (Mohan & Rafferty 2015). The multi-scale setting assumes that the emission can be modeled as a collection of components at a variety of spatial scales, hence, this setting is necessary to account for the extended emission. We used the `Briggs` weighting scheme with a robust parameter of 0.

Following initial imaging, we performed self-calibration with a few rounds of phase-only calibration and checked that the

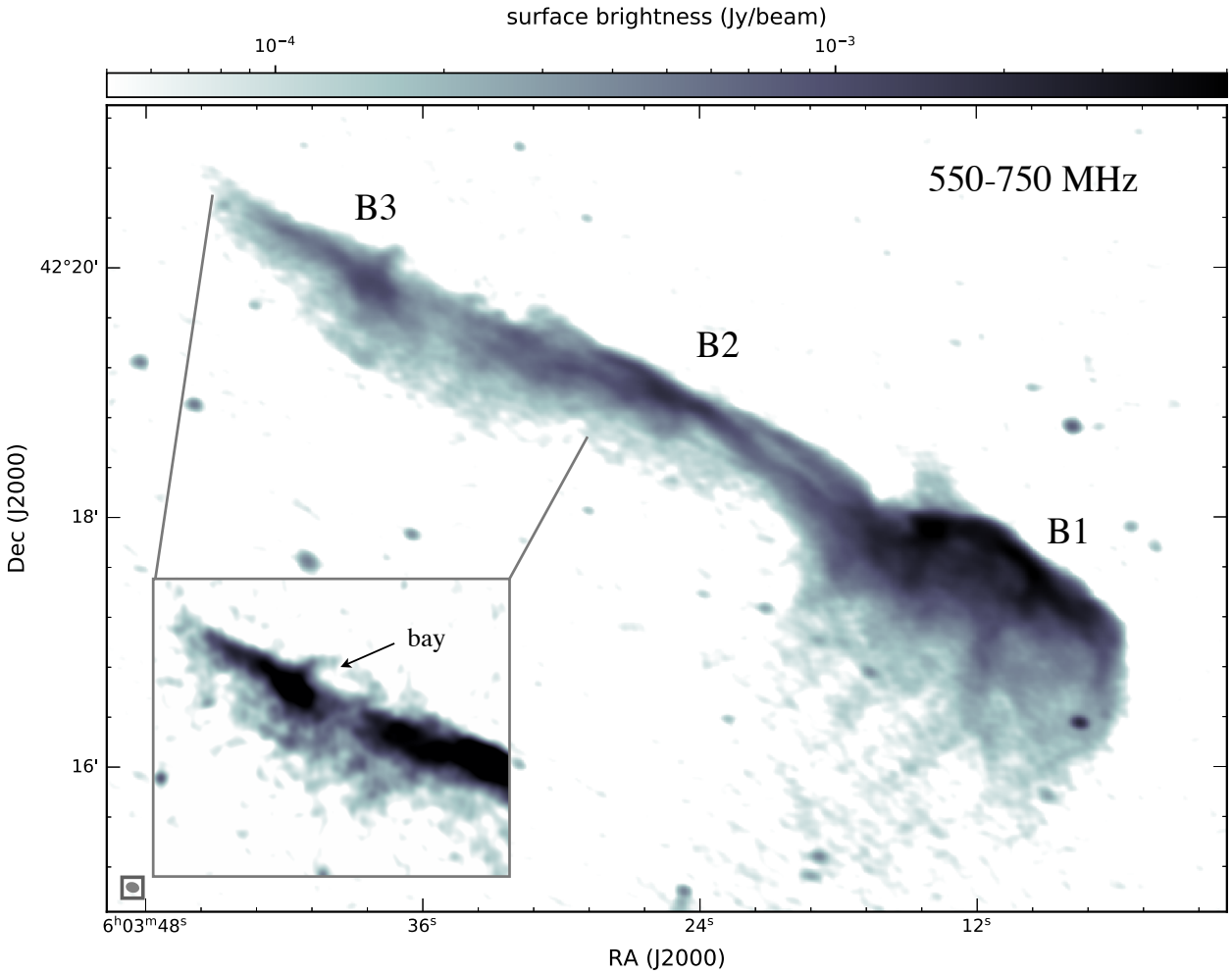


Fig. 2. High resolution uGMRT image of the Toothbrush relic confirming the complex filamentary structures visible at 1-2 GHz (Rajpurohit et al. 2018) also in the 550-750 MHz range. The beam size is indicated in the bottom left corner of the image. Inset show a low surface brightness emission, labelled as "bay", connecting the B2 region to B3. The image properties are given in Table 2, IM14.

model, to be included for self-calibration, did not have artifacts or negative components. We then ran a final round of amplitude-phase calibration. After deconvolving each configuration independently, we subtracted source A from the uv-data (for labeling see Fig.1. To speed up imaging, we subtracted in the uv-plane all sources outside the cluster region.

The final S-band deep Stokes I continuum images were made by combining the data from B and C configurations using `nterms=2` that reduced the noise level. The CASA task `widebandpbcor` was used to correct for the primary beam attenuation.

3.2. uGMRT observations

The GMRT observation of 1RXS J0603.3+4214 was carried out with upgraded GMRT (uGMRT) in band 4 (proposal code: 34_073). The data were recorded into 4096 channels covering a frequency range of 550-750 MHz with a sampling time of 8 seconds. All four polarization products were recorded. The primary calibrator 3C147 was included to correct for the bandpass and phase. For polarization calibration, the secondary calibrators 3C138 and 3C286 were observed. The 5 minutes scan on each of 3C84, 3C48, and 1407+284 were also recovered during the observing session.

The uGMRT data were calibrated with `CASA`, version 4.7.0. We split data into 4 sets, namely set1(channels 0−999), set2 (channels 1000−1999), set3 (channels 2000−2999), and set4 (channels 3000−4096). The data were first visually inspected for the presence of RFI where affected data were subsequently removed using `AOFlagger`. Initial phase calibration was performed using 3C147 and were subsequently used to compute parallel-hand delay. The primary calibrator 3C147, together with 3C138 and 3C286, were used for flux and bandpass calibration. We used the Perley & Butler (2013) extension to the Baars et al. (1977) scale for the absolute flux calibration. Applying the bandpass and delay solutions, we proceeded with the gain calibration for 3C147, 3C138, and 3C286. All relevant solution tables were applied to the target field. Each set was then averaged by a factor of 4 in frequency. The averaging of the uGMRT and VLA data was done to permit the RM-Synthesis and QU-fitting. The polarization results of the VLA and uGMRT observations of the 1RXS J0603.3+4214 field will be presented in a subsequent paper (Rajpurohit et al. in prep).

After this, we combined all data (i.e., set1, set2, set3, and set4 data). Several rounds of phase self-calibration were carried out on the combined data followed by two final rounds of amplitude and phase self-calibration. We visually inspected the self-calibration solutions and manually flagged some additional data. De-convolution was performed with `nterms=2`,

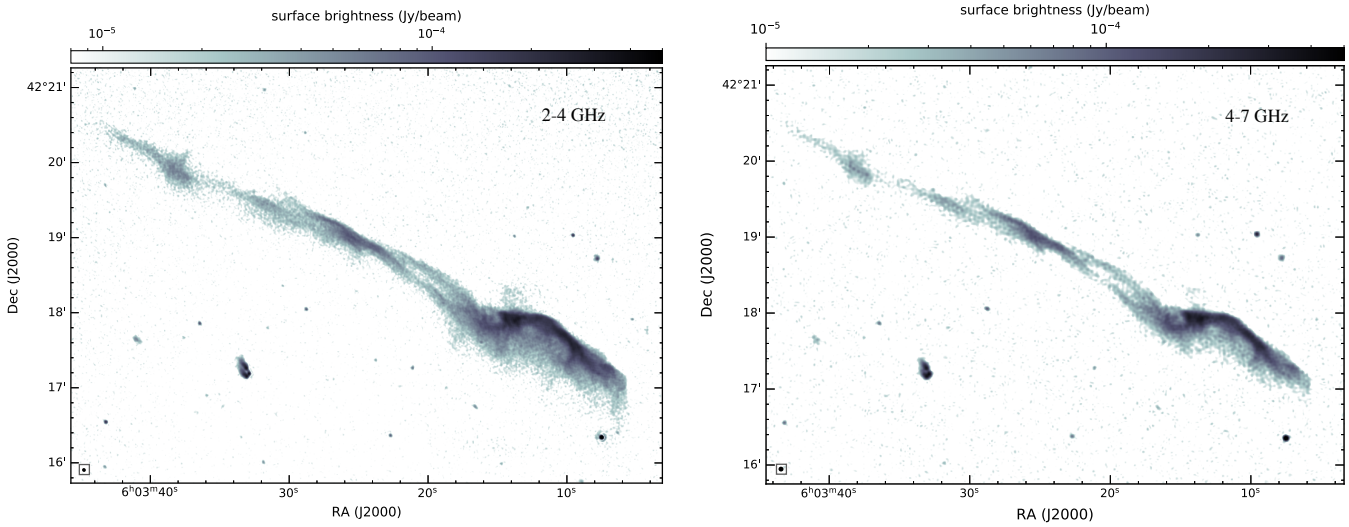


Fig. 3. S-band (2-4 GHz) and C-band (4-7 GHz) high resolution image of the Toothbrush relic. Most of the large scale filaments are evidently recovered up to 7 GHz. The beam size are indicated in the bottom left corner of the image. The image properties are given in Table 2, IM4 and IM1.

`wprojplanes`=500, using `Briggs` weighting with robust parameter 0.

4. Results: Continuum images

We show in Fig. 1 the resulting total intensity uGMRT (550-750 MHz) and S-band (2-4 GHz) radio continuum images of 1RXS J0603.3+4214. These images are created with different uv-tapers to emphasize the radio emission on various spatial scales. The sources are labeled following van Weeren et al. (2012) and Rajpurohit et al. (2018). An overview of the properties of the diffuse radio sources in the cluster is given in Table 3.

4.1. The Toothbrush relic

The most prominent source in the 1RXS J0603.3+4214 field is the large toothbrush shaped relic which is detected in all of the radio maps. The high resolution deep wideband images of the Toothbrush relic are shown from Fig. 2 to Fig. 3. The synthesized beams and sensitivities of these images are mentioned in Table 2.

Our new images manifest the variety of fine structures, as reported by Rajpurohit et al. (2018), in the form of arcs, streams, and filaments of enhanced surface brightness. In Fig. 2, we show our deep uGMRT $5\farcs0 \times 4\farcs8$ resolution image of the Toothbrush, with `Briggs` weighting and `robust`=0. Thanks to the wideband receivers, we reached to a noise level of 7.7 μ Jy beam^{-1}. The new uGMRT observations are sensitive to much lower surface brightness emission than the published 610 MHz GMRT image (van Weeren et al. 2012).

The new uGMRT image reveals all small and large scale filamentary structures reported by Rajpurohit et al. (2018) also in the 550-750 MHz range. It suggests that up to 2 GHz the radio synchrotron emission has the same spatial distribution. In terms of morphology, our uGMRT image is comparable to the published GMRT image.

Rajpurohit et al. (2018) also reported a tentative detection of a bridge like emission feature connecting the northern edge of B2 to an arc-shaped filament in the B3 region. In the uGMRT image, the emission is evidently visible, see Fig. 2 lower left, however, the emission appears to be disconnected from B3. We label this emission feature as the "bay". We do not find any cluster galaxy close to the "bay".

All identified filamentary features excluding the small-scale features, namely bristles, are also visible in the VLA S- and C-band images; see Fig. 3. At all three frequencies, the northern edge of the "brush" region, B1, is extremely sharp. We can set an upper limit to the width of the leading edge of the brush region of $2''$, which corresponds to 6.5 kpc. The largest linear size (LLS) of the Toothbrush relic remains almost the same, i.e., $\sim$ 1.9 Mpc, from 550 MHz to 8 GHz. However, the width decreases in the north-south direction with increasing frequency. The width of B1 at 550-750 MHz, S-band and C-band is 530 kpc, 327 kpc, and 243 kpc, respectively. This is expected for a source with a strong spectral index gradient across it.

In Fig. 4, we show a combined uGMRT (550-750 MHz), VLA L-band (1-2 MHz), and S-band (2-4 GHz) image of the Toothbrush. The image shows clearer filaments. Various components of the Toothbrush are labeled as in Rajpurohit et al. (2018).

The emission in the B1 region consists of bright short filaments, labeled as "bristles", with a width of 3-8 kpc. We note that the widths of the "bristles" are almost the same at the 550-750 MHz and the 1-2 GHz. The filaments in the B2 region are generally extended over considerable distances. The brightest region in B2 is at the intersection of double strand ("twist"). A low surface brightness emission, source M, to the northeast of B1 is visible at all three frequencies; see Fig. 1 and Fig. 2)

Our high resolution radio maps show filamentary features on various scales that are visible from 550 MHz to 8 GHz. In fact, radio relics when imaged at high resolution mostly show filamentary substructure. The origin of filaments that we discovered is challenging to explain. The observed filaments could be projections of substructures from a complex shaped shock front or may reflect variations of the electron acceleration efficiency and trace a fluctuating Mach number distribution internal to relics (Wittor et al. 2017). Also, they may illuminate regions where different magnetic field domains are forced to merge (Owen et al. 2014).

4.2. Relics E and D

The other two fainter relics E and D are well detected in the S-band images, Fig. 1. The LLS of both relics are similar to those observed below 2 GHz.

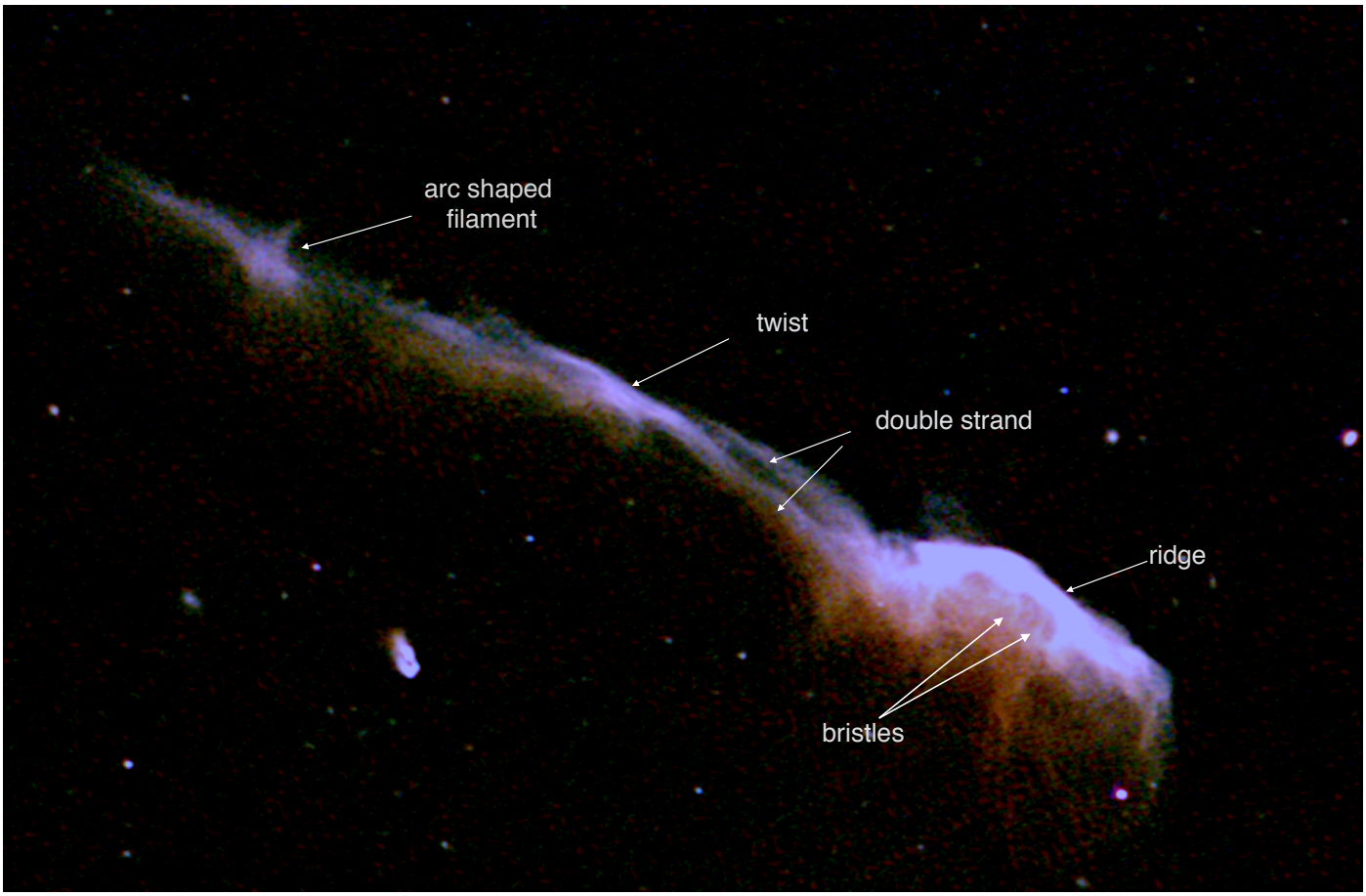


Fig. 4. Combined uGMRT (550-750 MHz), VLA L-band (1-2 GHz), and VLA S-band (2-4 GHz) image of the Toothbrush relic manifesting variety of small and large scale complex filamentary structures. The resolution of the uGMRT , the VLA L-band, and VLA S-band images are 3.″1, 1.″8, and 2.″0, respectively. The colors reflect the local spectral index variations within the relic, although there is not a 1:1 match.

The relic E is consists of two parts, E1 and E2. They are morphologically different. The E2 region of the relic E is fainter and more extended than the E2. There are recent observational examples which seem to show a connection between relics and active galactic nuclei (AGN), i.e, they provide evidence that the shock fronts re-accelerate CRe of a fossil population (Bonafede et al. 2012b; van Weeren et al. 2017a,b; Di Gennaro et al. 2018; Stuardi et al. 2019). We note that several radio sources are embedded in the relic E, however, we do not find any obvious connection to the relic.

4.3. Radio halo

Our new observations provide the first detailed image of the central halo emission in 1RXS J0603.3+4214 at 2-4 GHz. The halo emission is best highlighted in the low resolution images, see Fig. 1. The total extent of the halo emission is about 8′, corresponding to 1.7 Mpc at 3 GHz. It has low surface brightness (> 0.03 mJy beam^{-1}) and is extended along the merger axis.

The halo is also recovered in the 550-750 MHz uGMRT images, see Fig. 1 panel (a). The overall morphology and extent of the halo at 550-750 MHz and 2-4 GHz are similar to that observed by van Weeren et al. (2016) and Rajpurohit et al. (2018) at 150 MHz and 1.5 GHz, respectively. However, we note that at each frequency, the transition from the relic to the halo occurs at somewhat different locations. Towards high frequencies (>1.5 GHz), we find that there is a slight decrease in the surface brightness, apparently separating the relic and the halo emission; see Fig. 1 panel (d).

In Fig. 5 we show a combined LOFAR (120-180 MHz), VLA L-band (1-2 GHz), and VLA S-band (2-4 GHz) image. The image nicely show that the brush region of the Toothbrush extends and penetrates into the halo. We labelled this region as "relic+halo". We will argue in Sec 6.4 that there is an overlap between the relic and the halo emission.

Chandra observations of 1RXS J0603.3+4214 revealed a weak shock of $\mathcal{M} \sim 1.8$ at the southern edge of the halo (van Weeren et al. 2016). We denoted this region as "region S" in Fig. 7. It has been reported that the region S is possibly connected to the southern shock front, thus may have a different origin Rajpurohit et al. (2018).

Higher resolution L-band images by Rajpurohit et al. (2018) showed that there are around 32 discrete radio sources in the area covered by the halo emission. Most of these points sources are also visible at 2-4 GHz.

The flux density of the halo, including discrete sources, at 610 MHz and 3 GHz are $S_{610\,\mathrm{MHz}} = 141 \pm 17$ mJy and $S_{3\,\mathrm{GHz}} = 18 \pm 2$ mJy, respectively. This is the flux density for the entire halo, including the relic+halo and region S. The measured flux density at 610 MHz flux is significantly higher than the published narrow band GMRT observations.

Table 3. Properties of the diffuse radio emission in the cluster 1RXS J0603.3+4214 .

Source	VLA			uGMRT	LOFAR	LLS[†]	α
	C-band	S-band	L-band				
	$S_{6\,\mathrm{GHz}}$ mJy	$S_{3.0\,\mathrm{GHz}}$ mJy	$S_{1.5\,\mathrm{GHz}}$ mJy	$S_{650\,\mathrm{MHz}}$ mJy	$S_{150\,\mathrm{MHz}}$ mJy	Mpc	
relic B	68 ± 2	138 ± 4	310 ± 21	752 ± 78	4428 ± 423	∼ 1.9	−1.16 ± 0.02
halo C	-	10 ± 1	33 ± 3	48 ± 5	490 ± 56	∼ 1.6[‡]	−1.16 ± 0.04
relic D	-	1.4 ± 0.1	5 ± 1	15 ± 2	96 ± 12	∼ 0.3	
s relic E	-	3.1 ± 0.3	12 ± 1	26 ± 3	135 ± 19	∼ 1	
region S	-	1.9 ± 0.1	9 ± 1	23 ± 3	141 ± 15	∼ 0.7	

Notes. Flux densities were measured from 25″resolution images, created with uniform weighting and without any uv-cut. The regions where the flux densities were extracted are indicated in the left panel of Fig. 7. We assume an absolute flux scale uncertainty of 10% for the GMRT and LOFAR data, 4% for the VLA L-band, and 2.5% for the VLA S-, C-band data;[‡]size of the halo includes the "relic+halo" and region S. The spectral index values are obtained from images with an uvcut; see Sec. 5; [†]the largest linear size at 3 GHz; [†]size of the entire halo.

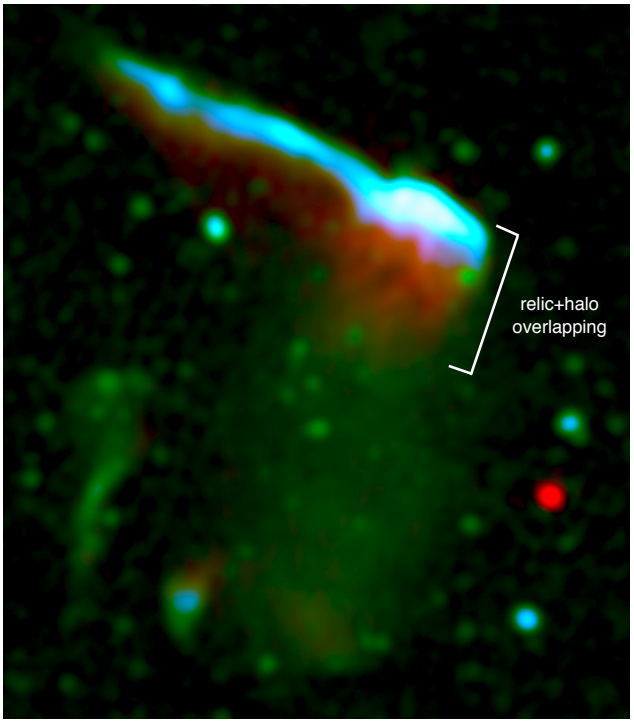


Fig. 5. Combined LOFAR (120-180 MHz), VLA L-band (1-2 GHz), and VLA S-band (2-4 GHz) image of the cluster at 15.7". The image clearly shows that B1 extends out of the relic and penetrates into the halo. As discussed in Sec 6.4, this is consistent with the superposition of the relic and the halo emission. The image properties are given in Table 2, IM10, IM13, and IM21.

5. Analysis of relics

To study the spectral characteristics of relics B, D, and E over a wide range of frequencies, we combined the deep VLA (2-8 GHz) and uGMRT (550-750 MHz) observations presented here with the previously presented ones at 1-2 GHz (Rajpurohit et al. 2018) and 150 MHz (van Weeren et al. 2016). In fact, the Toothbrush is the first relic where the radio interferometric observations over such a wide frequency range are available.

5.1. Flux density measurements

In order to derive reliable flux densities and spectral index maps, we imaged each data set with uniform weighting and convolved the final images to the same resolution. However, such images can only be produced if we have the same uv-coverage in each interferometric observation otherwise this results in a bias in the total flux density measurements of very extended sources.

The radio observations reported here are performed with different interferometers, each of which have different uv-coverages. The shortest baseline for the LOFAR, uGMRT, VLA L-band, VLA S-band, and VLA C-band data are 0.03 kλ, 0.2 kλ, 0.2 kλ, 0.3 kλ, and 0.4 kλ, respectively. To have the same spatial scale at all frequencies, we create images with a common lower uv-cut at 0.4 kλ. Here, 0.4 kλ is the well sampled baseline of the uGMRT and the VLA C-band data. This uv-cut is applied to the LOFAR and the VLA L- and S-band data. To reveal the spectral properties of different spatial scales, we tapered the images accordingly.

To measure flux densities, we create images at 8″ × 8″ resolution with a common inner uv-range mentioned in Sec. 5. We chose 8″resolution images for measuring the flux densities to: (1) avoid contamination from the halo emission in the "relic+halo" region. As mentioned by Rajpurohit et al. (2018) between 150-650 MHz, the "relic+halo" is dominated by B1 emission but in contrast between 1-4 GHz by the halo emission. Therefore, when determining the integrated spectrum this region is considered as the part of the toothbrush relic. The reason is, at 8″ resolution the low surface brightness halo emission does not contribute much to the relic B emission and will not significantly affect our flux density measurements; (2) since it increases the signal-to-noise radio in low surface brightness regions, in particular for B3 at high frequency, namely in C-band.

Radio relics usually contain a number of discrete sources, thus making an accurate measurement of the integrated spectra difficult. The contamination by discrete sources, therefore, needs to be subtracted from the total diffuse emission first. Luckily, the Toothbrush is not in close-by to any unrelated sources except source S1, see Fig. 1 panel (c). We do not subtract its flux contribution because the source is rather faint ($S_{1.5\,\mathrm{GHz}}$ = 1.8 ± 0.1m Jy), therefore, the contamination is not relevant.

The uncertainty in the flux density measurements are estimated as:

$$\Delta S = \sqrt{(F \cdot S_\nu)^2 + N_{\mathrm{beams}}\,(\sigma_{\mathrm{rms}})^2} \quad (1)$$

where F is an absolute flux calibration uncertainty, S_ν is the flux density, σ_{rms} is the RMS noise and N_{beams} is the number of beams. We assume absolute flux uncertainties of 4 % and 2.5 % for the VLA L-band and S-, C-band (Perley & Butler 2013), respectively. While for the uGMRT and the LOFAR data, assumed flux uncertainties is 10 % (Chandra et al. 2004; van Weeren et al. 2016).

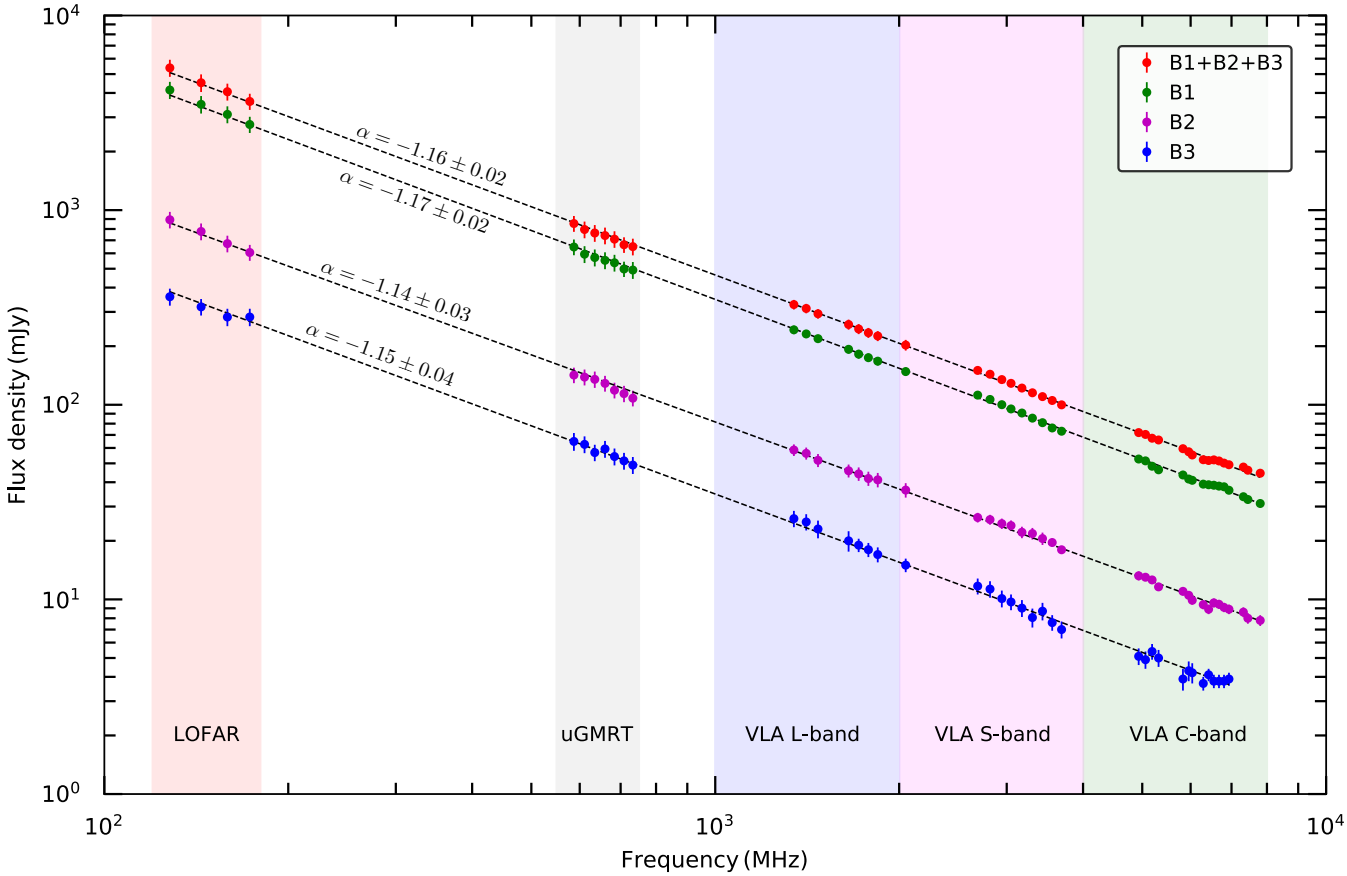


Fig. 6. *Left*: Integrated spectra of the main Toothbrush and subregions between 150 MHz and 8 GHz. Dashed lines are fitted power-law. The spectrum of the main Toothbrush is well described by a single power-law with slope $\alpha = -1.16 \pm 0.02$. We rule out any possibility of spectral steepening of the relic emission at any frequency below 8 GHz. Despite being located at different distances from the ICM, the B1, B2, and B2 spectra are remarkably identical. The flux densities are measured from 8″ resolution images, created using uniform weighting with a uv-cut at 0.4 k λ. The regions where the flux densities were extracted are indicated in the left panel of Fig. 7.

We compare our flux density measurements with values obtained with single dish observations that do not resolve out flux of extended sources. At 4.8 GHz, we measure a flux density of 83 ± 8 mJy which is higher than the measurement with Effelsberg at 4.85 GHz, namely 68 ± 5 mJy (Kierdorf et al. 2017). However, they noted that their value is possibly too low because of the insufficient size and low quality of the radio map. At 8 GHz, we measure a flux density of 52 ± 5 mJy which is consistent with the value obtained with the Effelsberg telescope at 8.35 GHz. Our interferometric high frequency measurements are in agreement with the results from the single dish telescope. This clearly indicates that our interferometric data is not affected by missing short baselines.

5.2. Integrated radio spectra of the Toothbrush

Detailed studies of the integrated spectra of radio relics, over a broad range of frequencies, serve as a useful measure of the energy distribution of the relativistic electrons. It provides insightful information to discriminate between competing models of particle acceleration currently proposed for radio relics.

The broadband interferometric observations allowed us to conduct the most sensitive study of the integrated spectrum of any relic up to date. To obtained the integrated spectra, we measure the flux density of the entire Toothbrush as well as in three subareas B1, B2, and B3. The regions where the flux densities were extracted are indicated in the left panel of Fig. 7. For all flux densities measurement of the relics, we use radio maps described in Sec. 5.1.

The most important and striking result of our analysis is shown in Fig. 6. We find that the integrated spectrum of the Toothbrush indeed follows a close power-law over close to 2 decades in frequency. Our results show for the first time that not only the main Toothbrush, the subregions (B1, B2, and B3) also exhibit power-laws.

A nearly perfect power-law spectrum across the Toothbrush up to 8 GHz is in contrast with that of an earlier study by Stroe et al. (2016). They reported radio interferometric observations of the Toothbrush from 150 MHz to 30 GHz and highlighted the steepening of the integrated spectrum beyond 2 GHz (from $\alpha = -1.00$ to -1.45). We note that the steepening in the flux density spectrum around 2.5 GHz was claimed on the basis of 16 GHz and 30 GHz radio interferometric observations. We found no evidence of spectral steepening and thus we completely rule out the possibility of steepening found by Stroe et al. (2016) below 8 GHz.

The integrated relic emission between 150 MHz to 8 GHz, has a spectral index of -1.16 ± 0.02. The integrated spectral index of the Toothbrush is consistent with our previous value of -1.16 ± 0.02 (Rajpurohit et al. 2018). Even more astounding, we find that the integrated spectral index of B1, B2 and B3 are remarkably close, namely $\alpha_{B1} = -1.17 \pm 0.02$, $\alpha_{B2} = -1.14 \pm 0.03$, and $\alpha_{B3} = -1.15 \pm 0.04$. It is surprising that B1, B2 and B3, despite being located in regions with very different ICM densities, show spectra with an almost identical slope. If the inte-

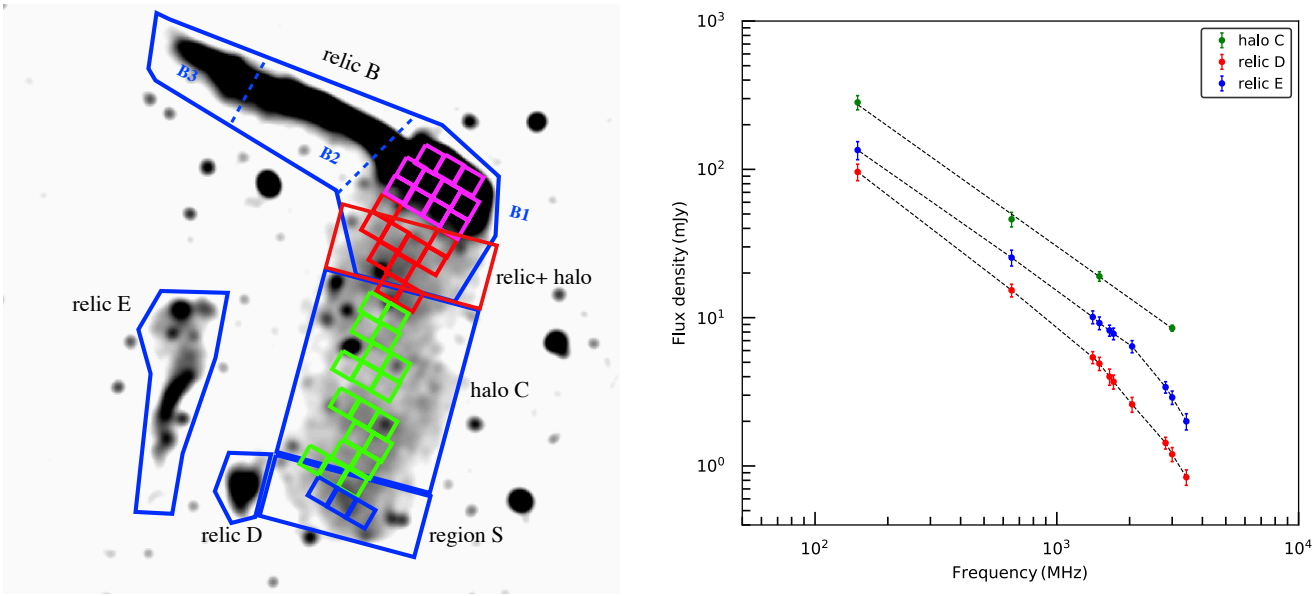


Fig. 7. *.Left*: VLA 15″resolution image depicting the regions where the integrated flux densities were measured. *Right*: Integrated spectra of the halo C and relics E and D. The spectrum of the halo C is well described by a single power-law spectrum. Relics E and D show spectral steepening beyond 1.5 GHz. The flux densities are measured from 15″ resolution images, created using uniform weighting with a uv-cut at 0.4 k λ.

grated spectral index reflects the Mach number of the shock, this seems to imply a remarkably uniform Mach number along the shock. We present a qualitative comparison with a recent numerical simulation of radio relics in Sec. 5.3.

Other than the Toothbrush, the integrated radio spectra over a wide range of frequencies are available only for five radio relics; the Sausage relic, the relic in A2256, Bullet cluster, ZwCl 0008.8+5215, and A1612 (Trasatti et al. 2015; Stroe et al. 2016; Kierdorf et al. 2017). Out of these five mentioned relics, a spectral steepening has been detected between 2-5 GHz for three relics, namely the Sausage relic, the relic in A2256, and Bullet cluster. In contrast to this, some authors reported no steepening in the integrated spectrum for the Sausage relic (Kierdorf et al. 2017; Loi et al. 2017).

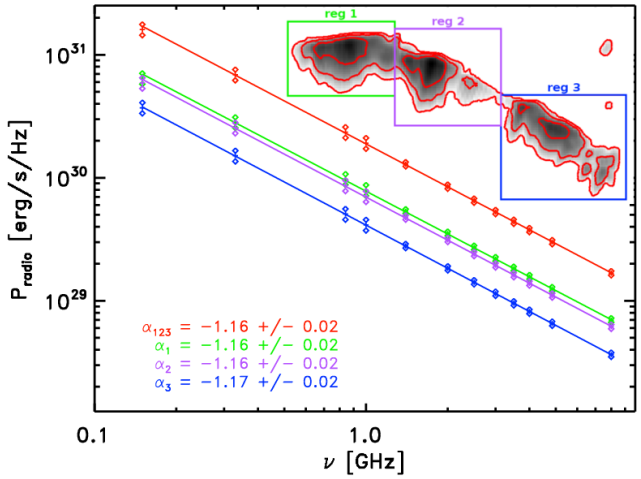


Fig. 8. Integrated spectra for the radio relic in a recent cosmological numerical simulation (Wittor et al. 2019). The red diamonds give the integrated spectrum of the whole relic, while the other diamonds give the spectra for the three subregions as in the inset (the color map gives the total intensity of the radio emission at 1.4 GHz. The simulated relic is ≈ 1.2 Mpc in size.

There are several reasons that may have led to the these differing results. The integrated spectra of these relics are derived from combining single-dish observations at high frequency (mostly above about 4 GHz) and interferometric observations at low frequencies (mostly below about 1.4 GHz). While interferometric measurements might underestimate the flux density as a result of missing short spacings, single-dish measurements lack resolution that might result in overestimate of the flux density owing to source confusion. Hence it remains unclear if the integrated spectrum of these three relics are curved at high frequencies or not.

According to DSA theory, in the equilibrium state, a shock of Mach number $\mathcal{M}$ generates a population of relativistic electrons with a power-law distribution in momentum (see e.g. Blandford & Eichler 1987). The resulting overall radio spectrum is a power law as well. The spectral index $\alpha_{\rm int}$ of the integrated spectrum is related to the Mach number according to

$$\mathcal{M} = \sqrt{\frac{\alpha_{\rm int} - 1}{\alpha_{\rm int} + 1}}, \tag{2}$$

For a stationary shock in the ICM, i.e. the electron cooling time is much shorter than the time scale on which the shock strengths or geometry changes, the integrated spectrum, is by 0.5 steeper than the injection spectrum ($\alpha_{\rm inj}$):

$$\alpha_{\rm int} = \alpha_{\rm inj} - 0.5. \tag{3}$$

Our integrated spectral index of the Toothbrush is consistent with the DSA approximation (Equation 3), where the radio spectrum is a power law with spectral index steeper than −1.

Moreover, we find that at most of the locations within B1, B2, and B3, the local spectrum is a "power-law" between 150 MHz and 8 GHz, whose slope varies systemically with distance from the shock. There is thus spectral steepening with little or any of the spectral curvature required by radiation losses in a relatively homogeneous environment. Inhomogeneities, in some combination of magnetic field strengths, Mach number and projections effects, will broaden the spectra and may be responsible for producing the locally varying power laws.

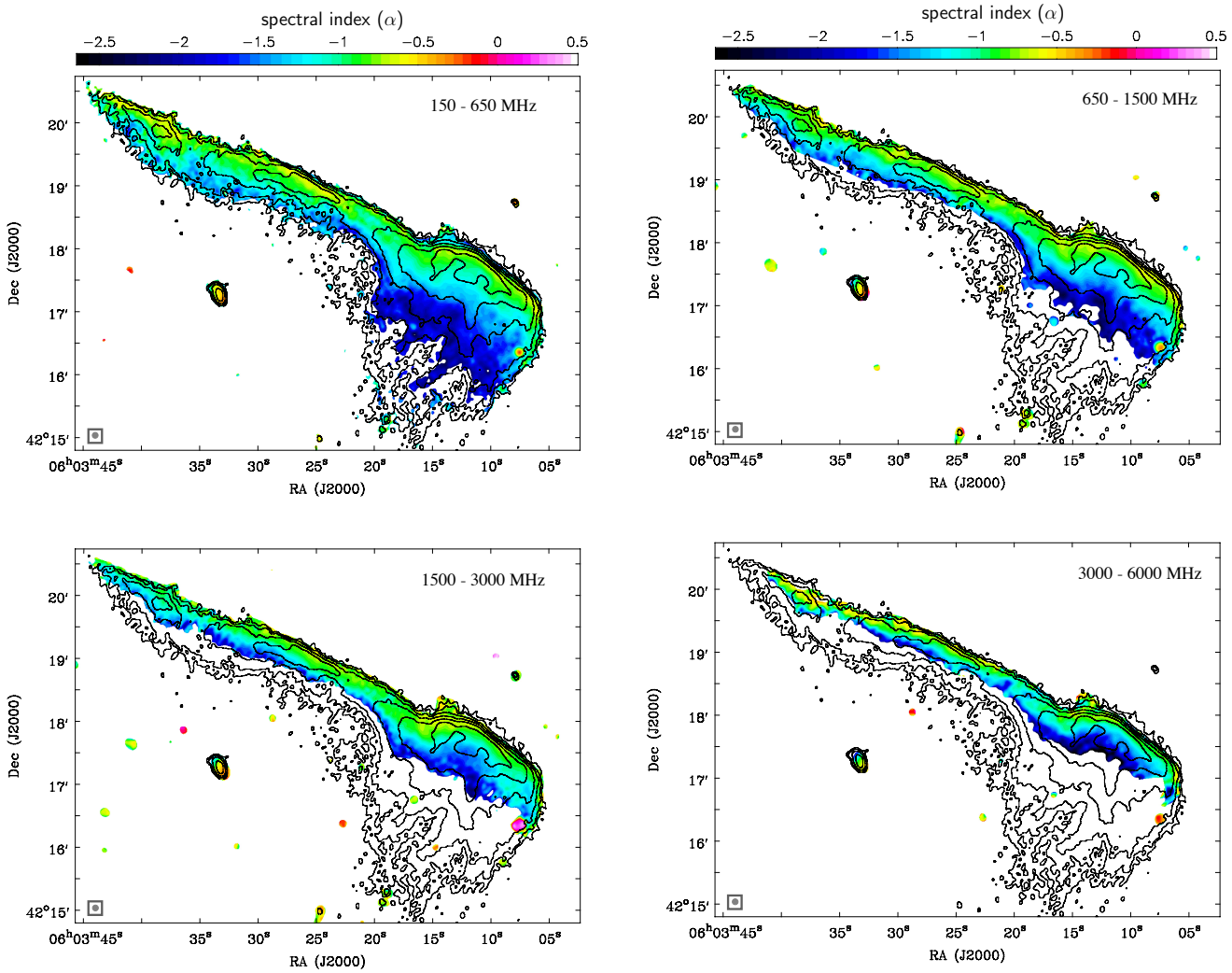


Fig. 9. Spectral index maps of the Toothbrush showing remarkably uniform spectral index gradient up to 6 GHz. *Left:* low frequency spectral index maps between 150 to 1500 MHz. *Right:* high frequency spectral index maps between 1.5 to 6 GHz. In all maps, contour levels are drawn at $[1, 2, 4, 8, \ldots] \times 4\,\sigma_{\rm rms}$ and are from the 150 MHz LOFAR image. These maps were created using the IM3, IM7, IM12, IM16 and IM20 (see Table 2 for image properties).

To derive the integrated spectrum of the relic E, we first subtract the flux density contribution from several discrete sources embedded in the relic. The resultant spectrum is shown in the right panel of Fig. 7, along with that of relic D. Unlike the Toothbrush, the overall spectra of relics E and D steepen at high frequencies.

5.3. Comparison with numerical simulations

At face value, it seems surprising that a single Mach number can characterize the entire shock surface across such a large distance. Numerical studies have indeed consistently reported that at least at the resolution probed by recent simulations and within their rather simplistic physical model, a rather broad distribution of shock strength is expected for merger shocks (e.g. Hoeft et al. 2011; Skillman et al. 2013; Ha et al. 2018; Wittor et al. 2019).

To investigate this issue in more detail, we computed the integrated emission spectra for a simulated radio relic, recently studied by Wittor et al. (2019). We remark that this simulation is not meant to reproduce the real Toothbrush relic, as the morphology of the simulated emission, see Fig. 8, and the properties of the host cluster are different from the 1RXSJ0603.3+4214 case. However, Wittor et al. (2019) presented the most detailed modeling of radio relic emission to date in numerical simulations, using an ENZO-MHD simulation with a maximum resolution of ≈ 4 kpc (Domínguez-Fernández et al. 2019). Unlike in previous studies, it models not only the injection of electrons by DSA, but also the time-dependent downstream cooling behind the shock edge.

The simulated relic forms in a $M_{100} \sim 10^{15} M_{\odot}$ galaxy cluster after a major merger at $z \approx 0.2$. It is located at a distance of ~ 1.7 Mpc from the cluster center and is ≈ 1.2 Mpc long (extending ≈ 500 kpc along the line of sight). The 3-dimensional distribution of the Mach numbers at the shock is broad, namely $2 \leq \mathcal{M} \leq 4$. The magnetic field strength at the relic is in the range $0.1\ \mu\text{G} \leq \text{B} \leq 2\ \mu\text{G}$, with a radio-weighted mean value of $\approx 1.05\ \mu$G. The total radio power of the relic, including the effect of shock re-accelerated electrons, is $\approx 10^{30}$ erg s^{-1} Hz^{-1} at 1.4 GHz. Thus, we can sum over all the simulated emission at different frequencies, to derive a simulated spectral distribution expected from the propagation of a merger shock in a clumpy ICM with self-consistent magnetic field structures. We computed the total integrated spectrum for the entire simulated relic across the same range of frequency of the real Toothbrush

observations, as well as integrated spectra for three different subregions of the simulation, as shown in the inset of Fig. 8.

Note that these regions show very different dynamical properties and magnetic field topologies as detailed in Sect. 3.6 of Wittor et al. (2019). We computed the spectral slope of the emission for each different patch (see inset in Fig. 8) with a simple least square fit, assuming a 10% uncertainty for flux below 1.4 GHz and 4 % at 1.4 GHz and above, similar to the real observation.

The simulation shows an intriguing similar spectral index, i.e. $\sim -1.16 \pm 0.02$ to the Toothbrush spectra (see Fig. 9). This is true for the separate regions of the simulated relic, as well as for the who.e in the three investigated regions as well as for the whole relic. Just as for the observations, it is remarkable that the spectra in the simulations are so similar in the different regions, despite the $\sim$ 1.2 Mpc extension of the relic and its clumpy morphology. This is at variance with what one might expect from the significant variations of Mach number at the shock front typically found in simulations (Hoeft et al. 2011; Skillman et al. 2013; Ha et al. 2018; Wittor et al. 2019). The combined effects of local variations in Mach number, 3D magnetic field fluctuations along the line of sight, the curved surfaces of realistic shocks, and the finite extension of the downstream cooling region of electrons can indeed conspire to broaden the individual spectral contributions and to converge on a very narrow range of power laws. In addition, it seems that the tail of the Mach number distribution, see e.g. Fig. 4 in Wittor et al. (2019) and Fig. 3 in Hoeft et al. (2011), determines the average spectral index. Of course, while this first comparison can qualitatively explain the very narrow distribution of spectral indices in the Toothbrush relic, a larger statistics of simulations and improved aging models for relativistic electrons are needed in order to fully explain the surprisingly straight spectrum of the Toothbrush.

5.4. Spectral index and Curvature

We examined the variations in spectral index and spectral shape across the relics to look for signatures of particle injection and energy losses. The difficulty in such spectral aging studies is that the curvature in the spectrum is very gradual, requiring sensitive observations to be made over a large frequency range at matched spatial resolution. The large size and high flux density of the Toothbrush allowed this type of analysis.

We created spectral index maps at the highest possible common resolution at all frequencies, i.e., at $5\farcs5 \times 5\farcs5$. The same maps are used to create radio color-color diagrams. Since conditions in the relic are highly inhomogeneous, the high resolution allows us to minimize the mixing within a single beam of emission with different spectral properties. For imaging we used a common lower uv-cut and a uniform weighting scheme, see Sec. 5.1 for details. Due to different uv-coverages of the LOFAR, uGMRT and VLA data, the resulting images had slightly different resolutions, so we convolved them all to a common, $5\farcs5 \times 5\farcs5$. For spectral indices between maps at two frequencies, we performed the calculation only for pixels with a flux density above 4.5 $\sigma_{\rm rms}$ in both maps.

The resultant spectral index maps of the Toothbrush at different pairs of frequencies are shown in Fig. 9. Overall the spectral index maps show remarkably similar spectral steepening towards the cluster center. The spectral index trends along the entire relic appear uniform between frequencies of 150 MHz to 6 GHz.

We find that the inferred "injection" spectral index at the outer edge of the relic, where acceleration is presumed to be actively happening, is $-0.65 \leq \alpha_{\rm inj} \leq -0.80$ from 150 MHz to 6 GHz. These values of injection index corresponds to Mach numbers in the range $2.8 \leq \mathcal{M} \leq 3.8$. This number is consistent with the injection index inferred from the integrated spectra, $-1.16+0.5 = -0.66$ (from Equation 3). Variations in the inferred injection index along the relic, at $5\farcs5 \times 5\farcs5$ resolution, reveal larger variations than seen in the integrated spectra over much larger regions, a direct indicator of small scale inhomogeneities.

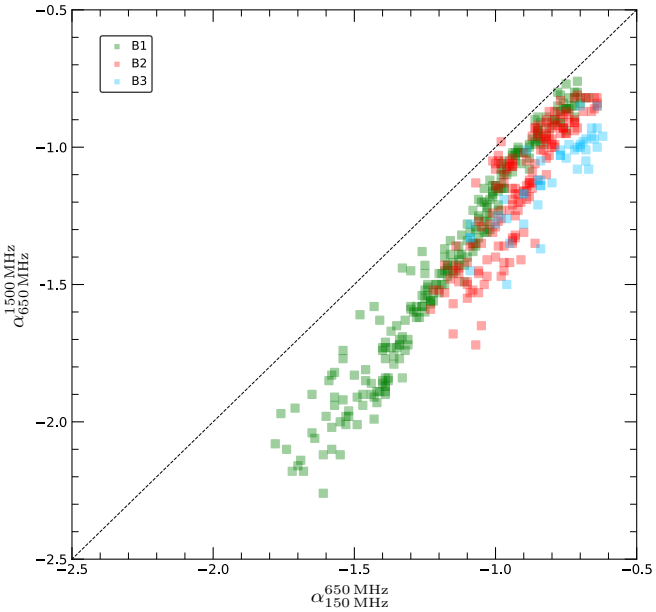


Fig. 10. Color-color diagram of the Toothbrush relic made at $5\farcs5$ resolution. The curves appears slightly different for B1, B2 and B3. Only B1 seems to trace out single and continuous curve. Spectral index values were extracted from maps created using the IM6, IM11, IM15, and IM19 (see Table 2 for image properties).

The detailed study of the evolution of the relativistic electron population responsible for the synchrotron emission provides critical information concerning the physical conditions in the source emitting regions. One commonly used fiducial spectral shape is the so-called "KP" spectrum, which assumes a single injection of particles, followed by radiative losses, with no pitch-angle scattering (Kardashev 1962; Pacholczyk 1970). An alternative model, the Jaffe and Perola (JP) model allows pitch angle scattering leading to a sharper cutoff at high frequencies (Jaffe & Perola 1973). Other models include continuous injection (CI) that considers a continuous fresh supply of injected electrons with a power-law distribution (Pacholczyk 1970) and an extension to the JP model, known as KGJP, that include a finite time of particle injection (Komissarov & Gubanov 1994).

To discriminate between different theoretical synchrotron spectral models, we employed the color-color plots described by Katz-Stone et al. (1993); Rudnick et al. (1994); van Weeren et al. (2012); Stroe et al. (2013). The shape of the color-color curve is an important indicator of the physical process taking place at the emitting region. This shape is conserved with respect to changes in the magnetic field or radiative losses, as long as there is no additional modification of the distribution of relativistic electrons. In addition, the color-color plots are useful for distinguishing source regions with different properties. At higher resolutions, it may be possible to minimize the effects of inhomogeneities, and determine the intrinsic shape of the spectrum for isolated components.

van Weeren et al. (2012) studied the color-color diagram of the Toothbrush using three frequencies; 610 MHz, 1.3 GHz, and

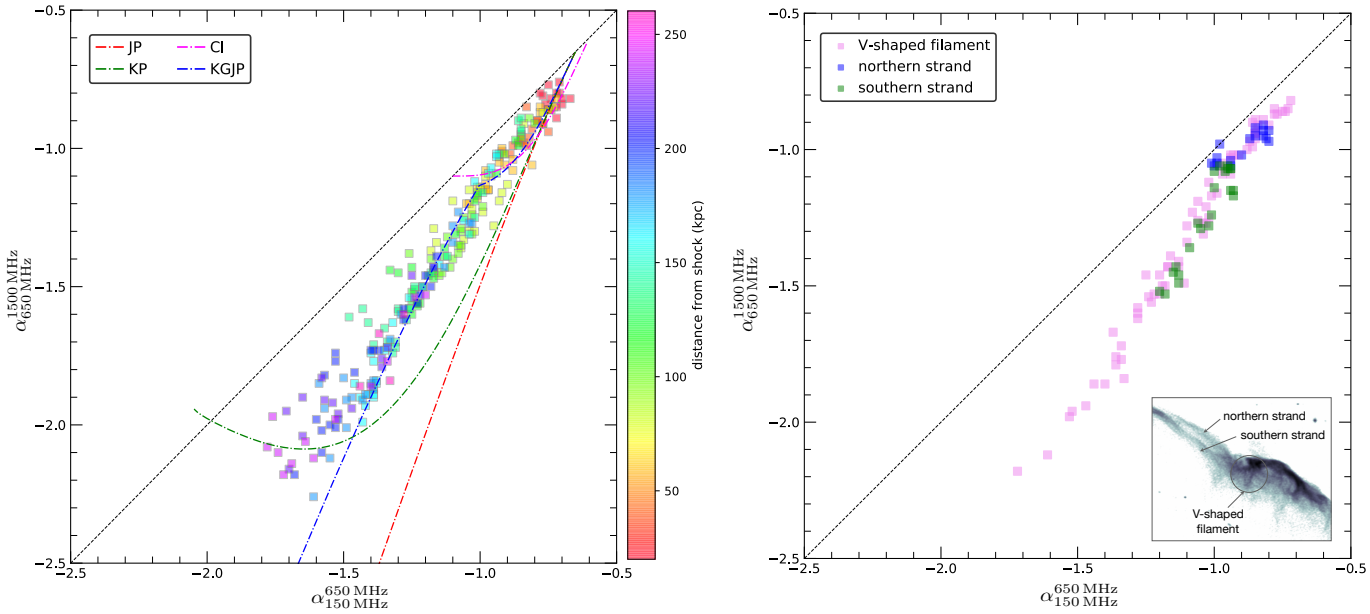


Fig. 11. *Left*: Color-color diagram for B1 superimposed with the JP (red), KP (green), and KGJP (blue) spectral aging models obtained with $\alpha_{\rm inj} = -0.65$. The CI (magenta) fit is obtained with $\alpha_{\rm inj} = -0.60$. No single one of these aging models can describe the entire spectral shape. *Right*: Color-color diagram of filaments in the Toothbrush, implying that individual filaments have different shapes. Spectral index values were extracted from maps created using the IM6, IM11, IM15, and IM19 (see Table 2 for image properties).

2.3 GHz. They found that the KGJP model provides a good fit for the entire Toothbrush. We extend the color-color analysis to smaller regions by utilizing high resolution maps and using 150 MHz, 650 MHz and 1.5 GHz data. We do not use the S- and C-band data because the width of the Toothbrush, in particular B1, decreases at high frequencies, thereby restricting the downstream areas where relativistic electrons can be observed as they age, for e.g., for B1 it becomes $\lesssim$ 123 kpc. For low frequencies, we use our spectral index map created between 150 MHz and 610 MHz while for the high frequencies between 610 MHz and 1.5 GHz (see Fig. 9).

The resultant color-color plot for the Toothbrush is shown in Fig. 10. The color-color plots are similar to the spectral curvature maps, with the curvature being the difference between the low and high spectral indices. A clear trend of increasing curvature, which was also detected by van Weeren et al. (2012), is visible in the plot. The shape in color-color plane is similar to the one reported by van Weeren et al. (2012), although they used different sets of frequencies. However, we find that the spectral shapes of B1, B2, and B3 are slightly different. In addition, we note an apparent shift for the B1, B2 and B3 regions, which could be the signature of slightly different injection indices.

In Fig. 11, we show a separate color-color plot for B1 and for the filaments in B2. The standard theoretical curves are superimposed on the color-color plot. The resultant plots reveal interesting details:

- B1 region: shows a single well defined locus of points in the color-color diagram. The single continuous distribution suggests that B1 has a single spectral shape that can describe the distribution everywhere in this region. We already see a steepening across the "ridge" (up to 50 kpc), see the left panel of Fig. 11. However, the conventional theoretical curves (JP, KP and CI) are seen to be a poor fit for the observed shape so there is likely some change in the physical conditions or processes downstream from the shock front which are not captured in the simple models.
  We rule out the KP model as the data points do not fit even for a small range; neither do we see any hint of the curve turning back to the $\alpha^{1.5\,\mathrm{GHz}}_{650\,\mathrm{MHz}} = \alpha^{650\,\mathrm{MHz}}_{150\,\mathrm{MHz}}$ line. The observed curve is also different than the continuous injection model because CI model only steepens according to Eq. 3. We see an increasing curvature trend from the shock front, but less quickly than the JP curve, implying a slower than exponential cutoff to the electron and synchrotron distributions.
  The KGJP model can be understood as a continuous sum of JP events with different ageing, which would produce such broadening. As reported by van Weeren et al. (2012), the KGJP model provides a good fit to the data but only for a certain distances from the shock front. One possible explanation can be projection effects. As one progresses further downstream, the emission becomes progressively more affected by projection effects. No single one of these models can describe the entire spectral shape.
  The color-color diagrams are useful to give constraints on the injection spectrum. As the spectra approach a power law at low frequencies, the locus of points in the color-color diagram intersects the power law line, where the position along the $\alpha^{1.5\,\mathrm{GHz}}_{650\,\mathrm{MHz}} = \alpha^{650\,\mathrm{MHz}}_{150\,\mathrm{MHz}}$ line (black dashed) is determined by the slope of the power law. For B1, our data indicate a low frequency index between the $\alpha_{\rm inj} = -0.65$ and $\alpha_{\rm inj} = -0.70$ curves.
- Filaments: The individual filaments in the Toothbrush show different shapes, see the right panel of Fig 11. This imply that different conditions in the different filaments are one significant contributor to the inhomogeneities.

The spectral index maps of relics E and D do not show a strong spectral index gradient as a function of position, see Fig. 13. To investigate whether they show any sign of spectral curvature, like the Toothbrush, we created a color-color diagram, using the spectral index extracted from 15.7″ (i.e., the beam size) boxes covering the relic E and relic D, see Fig. 12. The regions are shown in the inset of the bottom right corner.

We find that there are two different regions in the relic E. The points extracted across the E1 (magenta) part fall along the power-law ($\alpha^{650\,\mathrm{MHz}}_{150\,\mathrm{MHz}} = \alpha^{3\,\mathrm{GHz}}_{1.5\,\mathrm{GHz}}$) line, suggesting that at these locations there is a very broad spectrum, approaching a power law. On the other hand, for the E2 region (red) the spectra are curved, i.e., the points below the power law line. Such a curved spectra could be due to aging. From the color-color it is evident that E1 and E2 are different regions, with different processes going on. It remains an open question why the relic E shows such a distribution.

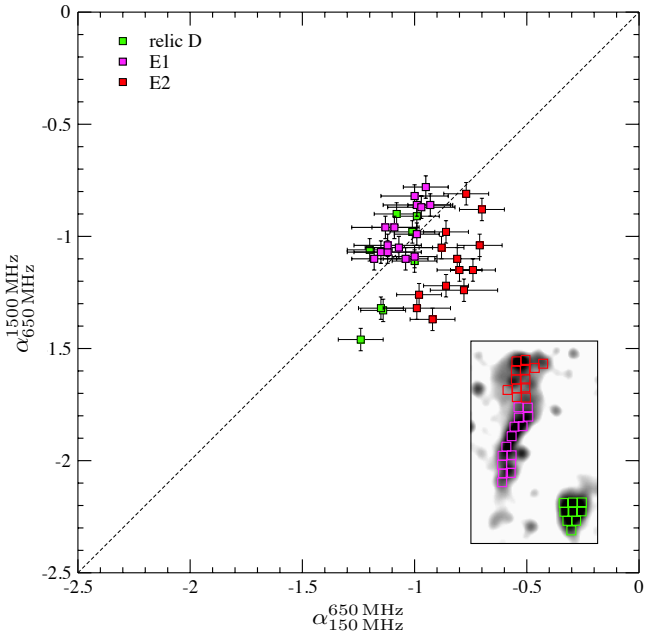


Fig. 12. Color-color diagram of relics E and D. Spectral index values were extracted from maps created using the IM10, IM13, IM18, and IM21 (see Table 2 for image properties)

It is interesting that the relics in 1RXSJ0603.3+4214 show different spectral properties. While the Toothbrush shows a strong spectral index gradient, no strong spectral gradient is seen across the relic E. The integrated spectrum of the Toothbrush follows a single power law but the relic E instead shows a spectral break at high frequencies.

5.5. Resolving discrepancies in the radio derived Mach numbers

From radio observations, the Mach number of a shock can be estimated using different methods, namely from the integrated spectrum, resolved spectral index maps and radio color-color diagrams. However, there is a claimed discrepancy between the Mach numbers obtained using these three methods (Hoang et al. 2017; Di Gennaro et al. 2018).

In the literature, most of the Mach numbers of relics derived from radio observations are estimated from the integrated spectral index. We obtained an integrated spectrum index $\alpha_{\mathrm{int}} = -1.16 \pm 0.02$ for the Toothbrush which corresponds to a Mach number of $\sim$ 3.7. From our spatially resolved spectral index maps between 150 MHz to 6 GHz, we find that the injection index is mainly in the range $-0.65 \leq \alpha_{\mathrm{inj}} \leq -0.80$. This corresponds to a Mach number in the range $2.8 \leq \mathcal{M} \leq 3.8$.

The color-color diagrams may provide a more reliable estimate (Di Gennaro et al. 2018) of the injection index than taking the flattest spectral index from a map. The color-color analysis of the Toothbrush suggests an injection index between -0.65 and -0.70. This injection index corresponds to a Mach number in the range $3.3 \leq \mathcal{M} \leq 3.8$.

For the Toothbrush relic the Mach number obtained from the integrated spectrum, the spectral index maps, and the radio color-color diagram are similar. Moreover, the surface brightness profiles also suggest an injection index of -0.65 (Rajpurohit et al. 2018). Mach numbers derived via different methods from the radio emission of the Toothbrush are now all in reasonable agreement and do not show any significant discrepancy.

5.6. Radio luminosity vs. thermal energy content

The brush (B1) of the Toothbrush is very radio bright. It has been argued that the high luminosity of the Toothbrush –and of other radio relics as well– is only possible when a significant fraction of the kinetic energy flux through the shock front is channelled into the acceleration of relativistic electrons (CRe) (van Weeren et al. 2016; Botteon et al. 2019). If the CRe originate from diffusive shock acceleration (DSA) of thermal electrons this would require a very high acceleration efficiency; in case of weak magnetic fields and a weak shock, the luminosity can not be explained by the standard DSA scenario. The tension between the relic luminosity and the kinetic energy flux might be lowered assuming an upstream population of mildly relativistic electrons which requires less energy input to produce the observed synchrotron luminosity.

Since we have measured the spectrum of the Toothbrush over a wide frequency range, we can address this problem adopting a slightly different viewpoint and comparing the radio luminosity of the emitting volume to the thermal energy content of that volume *without* considering any particular acceleration mechanism.

A small ICM mass element downstream to the shock may emit at the frequency ν with the emissivity $\epsilon_\nu(t)$. Due to the radiative losses of the relativistic electrons the emissivity decreases with distance to the shock front. We simplify the profile and assume that the mass element emits with a constant emissivity ϵ_ν, from the time that it has just passed through the shock front to the time $t_{\mathrm{d}}(\nu)$. The time $t_{\mathrm{d}}(\nu)$, after which the emissivity drops to zero, is related to the frequency dependent downstream extent of the emitting volume by $d(\nu) = t_{\mathrm{d}}(\nu) \cdot v_{\mathrm{down}}$, where v_{down} denotes the relative speed of the downstream material with respect to the shock front. The luminosity of the entire emitting volume is given by $P_\nu = \epsilon_\nu \cdot A\, d(\nu)$, where A is the surface area of the shock front.

The synchrotron emission over all frequencies of a volume ΔV during the 'luminous period' $t_{\mathrm{d}}(\nu)$ is given by the integral

$$E_{\mathrm{sync}} = \Delta V \int \epsilon_\nu\, t_{\mathrm{d}}(\nu)\, \mathrm{d}\nu = \frac{\Delta V}{A\, v_{\mathrm{down}}} \int P_\nu\, \mathrm{d}\nu\,. \tag{4}$$

The ratio of the synchrotron emission to the thermal energy in the volume, $E_{\mathrm{th}} = \Delta V\, n\, \bar{e}$, amounts to

$$\frac{E_{\mathrm{sync}}}{E_{\mathrm{th}}} = \frac{\int P_\nu\, \mathrm{d}\nu}{A\, v_{\mathrm{down}}\, n\, \bar{e}}\,, \tag{5}$$

where n denotes the particle density and $\bar{e}$ the average thermal energy per particle. The rest-frame luminosity is related to the measured flux density S_ν by

$$P_\nu = 4\pi\, D_{\mathrm{L}}^2(z)\, (1+z)^{-(1+\alpha_{\mathrm{int}})}\, S_\nu\,, \tag{6}$$

where D_{L} denotes the luminosity distance.

We assume that the spectrum follows a power law in the observed frequency range with 210 mJy at 1.5 GHz and a spectral

slope $\alpha_{\rm int} = -1.16$. Furthermore, we adopt that a particle density in the downstream region of 10^{-4} cm^{-3}, an average energy per particle of 6 keV, and a shock surface area of (0.7 Mpc)^2.

Limiting the frequency integral in Equation 5 to only the observed range from 150 MHz to 8 GHz, we find a ratio $E_{\rm sync}/E_{\rm th} = 5 \times 10^{-3}$. The spectrum of the brush shows a perfect power law, with no indications for bending at low or high frequencies, see Fig. 6. Thus, according to the theory of synchrotron emissivity of monochromatic electrons (Rybicky et al. 1982), the observed power law shape of the emission spectrum also implies radio emission outside of the frequency range of the observations.

To estimate the minimum luminosity outside the observed frequency range we model the electron spectrum by assuming a constant momentum distribution up to a Lorentz factor $\gamma_{\rm knee}$, a power law momentum distribution from $\gamma_{\rm knee}$ to $\gamma_{\rm max}$, and no electrons with Lorentz factor above $\gamma_{\rm max}$. The shape is intended to mimic the distributions derived in Sarazin (1999). Assuming a magnetic field strength of 1 µG, we find that $\gamma_{\rm knee}$ has to be <3000 and $\gamma_{\rm max}$>10^5 to avoid that a clear bending of the spectrum within the observed frequency range becomes noticeable. This implies that at least the same amount of energy must be radiated via synchrotron emission outside of the observed frequency range. Therefore, the observed power law spectrum of the brush region implies that synchrotron radiation is equivalent to a loss of at least 1 % of the thermal energy.

It should be noted that this result depends neither on the actual acceleration process nor on the spectral energy distribution of the electrons. Relativistic electrons will also emit via the inverse Compton (IC) process. The ratio of synchrotron to IC losses is determined by the ratio of the energy densities of magnetic fields, $u_B = B^2/8\pi$, and Cosmic Microwave Background photons. The equivalent magnetic field of the latter is given by $B_{\rm CMB} = 3.24\,(1+z)^2$ µG. With a magnetic field B below $B_{\rm CMB}$ a significant fraction of the energy content in a volume ΔV would be emitted via IC emission. This would clearly affect the thermal evolution of the intra-cluster medium and would have an impact on the ICM evolution. Since such an effect has not been observed, low magnetic fields in the emission region of the relic can be excluded. This is in agreement with the non-detection of IC emission in hard X-ray. The analysis of recent Suzaku observations provides a lower limit for the magnetic field strength, namely 1.6 µG (Itahana et al. 2015).

6. Halo structure and spectrum analysis

The cluster shows low surface brightness radio emission with a morphology remarkably similar to the ICM distribution (van Weeren et al. 2016; Rajpurohit et al. 2018). Even if it is widely accepted that halos are related to ICM turbulence, details of their origins are not well understood. Our deep observations allow us to study the spectral properties of the radio halo over a wide frequency range and to assess the physical mechanisms (e.g. Brunetti et al. 2001) powering the radio emission.

6.1. Integrated spectrum of Halo C

In order to obtain the integrated radio spectra of the halo, we measure the flux densities from the 15″ radio maps, where the signal-to-noise ratio is high enough. To ensure that we recover flux on the same spatial scales for all frequncies, we again produced images with a common lower uv-cut of 0.4 kλ. The regions where the flux density is measured are indicated in the left panel of Fig. 7. Since the halo has a very low surface brightness, we average for each observation the entire bandwidth, as given in Table 3. The resulting integrated spectrum is shown in Fig. 7.

Remarkably, the halo shows a power law with no indications of a spectral steeping, similar to the Toothbrush relic, when we restrict the analysis to the main halo region without relic+halo and region S. The integrated radio halo emission in that region between 150 MHz and 3 GHz, has a spectral index of $\alpha_{\rm halo} = -1.16 \pm 0.04$, which is, even more surprisingly, identical to the integrated relic spectral index. This spectral index of the halo is in agreement with earlier studies (van Weeren et al. 2016; Rajpurohit et al. 2018). However, our results show for the first time that the halo follows indeed a power law over a wide frequency range. Such a wide frequency range spectral coverage is only available for a few other clusters (for a review see Feretti et al. 2012). Those reveal a large variety of integrated spectral indices and of spectral shapes. For instance, Thierbach et al. (2003) reported for the halo in the Coma cluster a significant steepening above about 1.5 GHz from about -1.2 to -2.3. In contrast, Liang et al. (2000) and Shimwell et al. (2014) found for the Bullet cluster a rather constant slope of -1.3. Interestingly, for the majority of halos with flux density measurements at more than two frequencies, as reported in Feretti et al. (2012), the integrated spectrum is either steep ($\lesssim -1.5$) or shows a steepening. Either the halo in 1RXS J0603.3+4214 is an unusual one, or the superb data quality permits us to do a much better job removing contaminating sources and distinct emission regions, such as region S and the relic-halo overlap region, as discussed in the next section.

6.2. Impact of SZ on the halo flux measurements?

To obtain a reliable radio spectrum for the halo, we need to consider possible corrections for the Sunyaev-Zeldovich (SZ) effect. The SZ effect is the distortion of the blackbody spectrum of the cosmic microwave background (CMB) due to inverse Compton scattering of CMB photons by free relativistic electrons in the ICM. As a result, the SZ effect can cause a *steepening* in the observed spectrum at $\nu > 1$ GHz, by lowering the zero point of the radio emission as a function of frequency (e.g Enßlin 2002; Brunetti et al. 2013; Stroe et al. 2014; Basu et al. 2016). Note that although the uniform CMB is not visible to the interferometers, small scale variations, such as those due to the SZ effect, will be detectable.

To check whether this is the case for our observation of the halo, we computed the expected level of the SZ decrement for the halo in 1RXS J0603.3+4214 with a realistic model of its gas density. We started by simulating a gas density and temperature distribution for a simple $\beta-$model, which we perturbed by introducing elongation along the direction connecting to the radio relic using an aspect ratio of 1:0.8, as well as a second massive sub-clump (with a total mass $M_{100} \approx 10^{14} M_{\odot}$), also described by a simple β-model and located at the approximate position of the X-ray substructure in 1RXS J0603.3+4214.

When integrating within a region corresponding to the halo C, we estimate a total SZ decrement at 3 GHz of −2.97 mJy. However, the total *observed* SZ decrement from the halo region is further reduced to −1.12 mJy, if we apply to the simulation the same ≥ 0.4 kλ uv-cut as in the observation. We investigated variations of this baseline model, i.e., by changing the mass of the second clump and/or its distance along the line of sight; these do not change our result. We thus conclude that the SZ decrement can only be ≤ 6 % of the radio flux density in the halo C region, and therefore it does not significantly contaminate the measured emission.

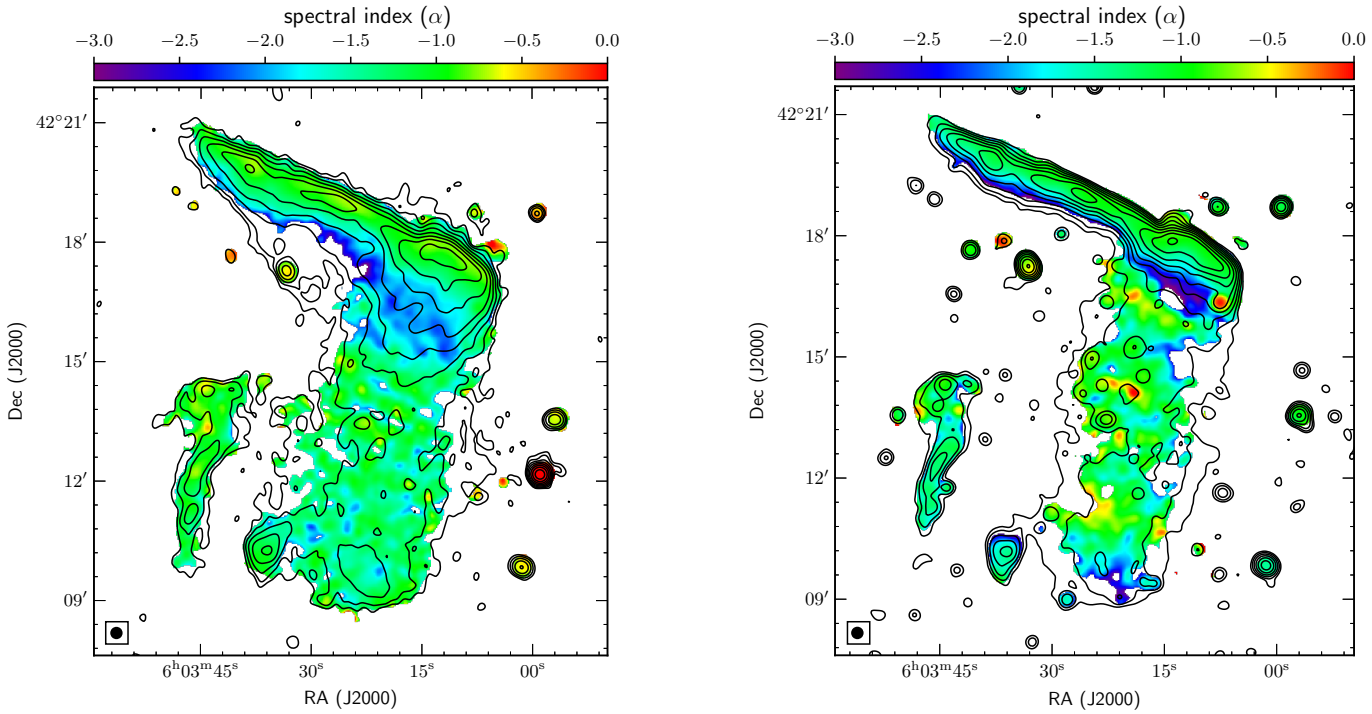


Fig. 13. Spectral index map of the radio halo in 1RXS J0603.3+4214 at 15.7″ resolution. *Left*: Low frequency (150 and 650 MHz) spectral index map. Contour levels are from the LOFAR and drawn at $\sqrt{[1, 2, 4, 8, \ldots]} \times 4\,\sigma_{\rm rms}$. *Right*: High frequency (1.5 and 3 GHz) spectral index map. Contours are from the VLA L-band and are drawn as in the left panel. These maps confirm a remarkable uniform spectral index distribution across the halo C between 150 MHz to 3 GHz. It is evident that the relic+halo region shows spectral steeping at low frequencies while there is a uniform spectral index distribution at high frequencies. These maps were created using the IM10, IM13, IM18, and IM21 (see Table 2 for image properties).

6.3. Spectral index and curvature distribution

We construct high and low frequency spectral index maps of the halo to investigate if there are any spatial variations across the radio halo. We use the images described in Sec. 6.1. The low frequency spectral index map is created using the 150 MHz and 650 MHz and the high frequency one between 1.5 GHz and 3 GHz. We do not subtract the extended or point like discrete sources embedded in the halo. Pixels with flux densities below $4\sigma_{\rm rms}$ were blanked.

Fig. 13 shows the high and low frequency spectral index map of the halo. As visible from both the high and low frequency spectral index maps, the spectral index across the central part of the halo, excluding the relic+halo and region S, is more or less uniform. To investigate it further, we employ the color-color diagram. The regions where the spectral indices were extracted are marked with green in the left panel of Fig. 7. The size of the each box is 15.7″, corresponding to physical sizes of about 57 kpc.

The resultant color-color distribution is shown in Fig. 14. The halo points (green) are indeed clustered near the black-dashed line. This is a clear signature of a power-law. It is evident from Fig. 14 that the spectral index of the halo is uniform over a broad range of frequencies. The is no indication of spectral curvature between 150 MHz and 3 GHz, even in regions as small as the selected boxes.

The radio halo shows a quite homogeneous surface brightness which correlates with the X-ray surface brightness (Rajpurohit et al. 2018). As shown above, the spectral index distribution is quite uniform and there is no indication of spectral curvature. The power-law spectrum over a large frequency range requires an electron momentum distribution which follows a power law as well at least for about one order of magnitude in momentum. In contrast to the relic, the power-law spectrum may arise from averaging along the line of sight through the ICM if the halo emission originates from volume filling turbulence. This would allow for local deviations from the average spectrum.

In the basic model explaining radio halos by turbulent re-acceleration of mildly relativist electrons, the acceleration is caused by electron scattering at magnetohydrodynamic waves which are excited as part of turbulent cascade (Brunetti et al. 2004; Brunetti & Jones 2014). We note, the simulated spectra, based on homogeneous conditions, rather produce curved spectra in the relevant electron momentum regime, a power law emission spectrum, as the observed one, is not expected from the basic model.

Adopting the critical frequency of synchrotron emission, we estimate that the Lorentz factor of the electrons emitting at the highest observed frequency for the halo, 3 GHz, amounts to $3 \cdot 10^4$ for a magnetic field of 1 µG. For these electrons the radiative loss time is as short as a few ten Myr (Sarazin 1999), which is of the same order or somewhat below the expected acceleration time scale (see e.g. Fig. 13 in Brunetti et al. 2004).

These timescales are much smaller compared to the crossing time of the halo region ($\sim$ 1 Gyr). This reinforces that the powering of radio emitting electrons by turbulent motions must happen throughout the radio halo volume, otherwise we would expect local variations in the curvature, even in projection. The acceleration timescale must also be significantly shorter than the cascade time along the Kolmogorov cascade, which also is of the order of the crossing time (e.g. Brunetti & Jones 2014). Therefore, the observed uniformity of the spectrum suggest that the halo emission is being being powered by an acceleration mechanism which is uniformly spread across the halo region. Why the

spectrum is homogeneously a power law remains to be understood.

6.4. Radio halo-relic connection

The halo and the "brush" region of the Toothbrush are connected by a region, denoted as "relic+halo" (for labelling see the left panel of Fig.7). A comparable example of the morphological connection between radio relic and halo was observed in CIZA J2242.8+5301 where the elongated halo is morphologically connected to the northern and the southern relic (Hoang et al. 2017).

We examine the spectral properties of radio emission in the apparent overlap regions to see if they are produced by a unique electron population or rather by the superposition of two separate particle populations along the line of sight. This is key to disentangling the complex chain of (re)acceleration events in the ICM (Hoang et al. 2017). The spectral index across the relic+halo region, between 150 MHz and 1.5 GHz, gradually flattens (from -2 to -1.2) over a distance of about 400 kpc and returns to being uniform in the rest of the halo region (van Weeren et al. 2016; Rajpurohit et al. 2018). It has been speculated that this spectral behavior indicates a possible connection between the shock and the turbulence (van Weeren et al. 2016; Hoang et al. 2017).

The spectral index variations across the relic+halo region appear different at low and high frequency. At low frequencies, where the relic emission dominates that of the halo, the spectral index across the relic+halo gradually steepens, see the left panel Fig. 13. Such a spectral steepening is expected in the downstream areas of relics when electrons undergo energy losses. In contrast, at high frequency, where the halo dominates, the relic+halo region shows a constant spectral index distribution like the rest of the halo, see the right panel Fig. 13.

The above trends suggest that both halo and relic emission is present in the overlap region, in different proportions at different frequencies. A clearer demonstration of this is seen in the color-color plot, where the relic+halo points (red points) lie above the power-law line. These points represent places in the spectrum with positive (convex) curvature, i.e., the spectrum is flatter at higher frequencies. This the expected behavior when there is a superposition of different emission spectra along the same line of sight. Although spectra with positive curvature can also be produced by a similarly-curved electron energy distribution, there is no need to invoke that here.

We find that for the regions with concave curvature, the range of $\alpha^{650\,\mathrm{MHz}}_{150\,\mathrm{MHz}}$ is -2.30 to -1.50 and $\alpha^{3\,\mathrm{GHz}}_{1.5\,\mathrm{GHz}}$ is -1.80 to -0.86. It is consistent that the steeper (lower frequency) emission component is from locally shock accelerated aged electrons (i.e., relic region) and the flatter (higher frequency) is due to the turbulent re-acceleration of electrons.

The southern edge of the radio halo in 1RXS J0603.3+4214 coincides with a shock front detected in *Chandra* observations(van Weeren et al. 2016). In a handful of clusters the radio halo emission seems to be bounded by cluster shock fronts (Markevitch et al. 2005; Brown & Rudnick 2011; Shimwell et al. 2014). The nature of these sharp edges is still unclear. Data points extracted across the region S (blue) lie below the power-law line. In the color-color plot, the region S appears different than the rest of the halo. The same region also appears distinct in the X-ray vs radio correlation (Rajpurohit et al. 2018), suggesting possible connection with the southern shock front, instead of a simple continuation of the halo.

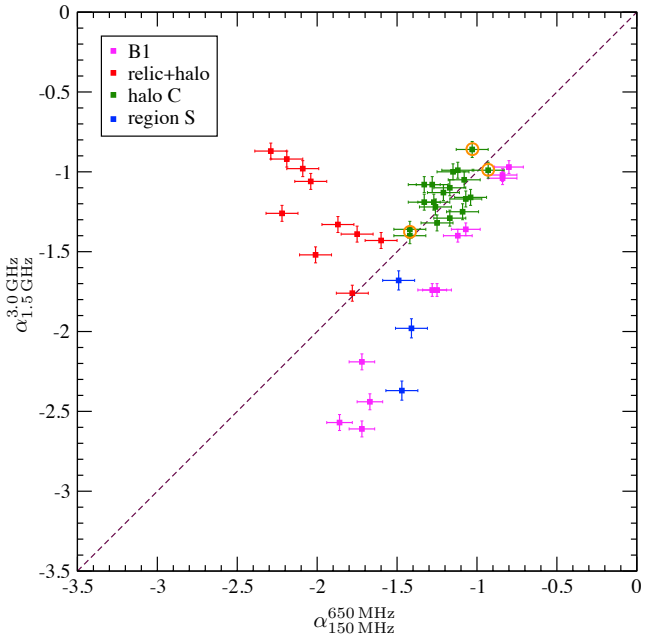


Fig. 14. Radio color-color diagram of the halo in 1RXS J0603.3+4214, using the spectral indices extracted in 15″ × 15″ boxes shown in the left panel of Fig. 7. The contaminated regions in the halo C are shown with orange circle. The relic+halo (red) indicate combined emission from the B1 region of the Toothbrush and the halo. The halo C points are clustered around the power law line, indicating no sign of spectral curvature. The relic+halo points lies in the concave part of the color-color plot, suggesting superposition of the halo and the relic emission.

6.5. Modeling of relic and halo integrated spectrum

We explore here the conditions leading to the integrated spectrum of relic B. This involves understanding the aging of the electrons, in particular in the downstream region of B1, where we have the best data. We model the aging of radio emitting particles under realistic yet simple conditions. We consider a simple "single-zone" model, assuming a single value of electron density, temperature and magnetic field across the entire B1 region. For simplicity, we also neglect the possible role of additional stochastic acceleration by cluster turbulence (e.g Donnert & Brunetti 2014) or the re-acceleration of fossil electrons in the shock downstream (e.g. Kang et al. 2012).

In our reference model, we fix the maximum length of the downstream cooling region, the downstream gas density and temperature to l_d = 855 kpc, $n_\mathrm{d} = 10^{-3}\mathrm{cm}^{-3}$ and $T_\mathrm{d} = 9.7\cdot10^{7}$K, respectively. For the maximum length l_d we adopted the largest length of downstream emission visible in the LOFAR image. The downstream magnetic field is set to B_d = 1.0 µG and the injection Mach number to $\mathcal{M}_\mathrm{inj}$ = 3.7. The energy flux that goes into the acceleration of electrons is given by

$$\Phi_e = \frac{1}{2}\xi_\mathrm{e} c_\mathrm{s}^3 \mathcal{M}_\mathrm{inj}^3 \rho_\mathrm{p} \cdot A^2, \quad (7)$$

where A is the assumed shock surface ($A \approx L^2$ where L is the length of B1 region), c_s and n_p are the pre-shock sound speed and gas density, respectively. These values are computed based on the standard jump conditions for a shock strength $\mathcal{M}_\mathrm{inj}$. The acceleration efficiency of electrons at the shock is set to a fix reference value of $\xi_\mathrm{e} \approx \cdot10^{-3}$, i.e., 0.1% of the ram kinetic energy of the shock goes into the acceleration of supra-thermal electrons. This value is in line with the value estimated previously in Equation 5, provided that ξ_e is referred to the shock kinetic

energy flux while in Sec. 5.6 we analyzed the ratio between the energy of relativistic electrons and the thermal gas.

In a simple 1-dimensional shock propagation, the radiative lifetime of electrons along the downstream region is $t_{\rm rad} = x_{\rm d}/v_{\rm s}$, where $v_{\rm s}$ is the shock velocity and $x_{\rm d} \leq l_{\rm d}$ is the 1-dimensional coordinate in the downstream direction, which we assume is pointing towards the cluster center. The time-dependent diffusion-loss equation of CRe within each integration step in our algorithm (e.g. Kardashev 1962; Sarazin 1999) is solved with the Chang & Cooper (1970) finite difference scheme. We use N=20,000 equal energy bins in the $10 \leq \gamma \leq 2 \cdot 10^5$ (γ is the Lorentz factor of electrons) energy range and an adaptive time stepping algorithm with 0.01 Myr $\leq \Delta$t $\leq$ 100 Myr. The overall radio spectrum in the shock downstream is obtained by numerically integrating the synchrotron emission from the distribution of accelerated particles (e.g. Ginzburg & Syrovatskii 1965), applying the JP aging model for simplicity (the general conclusions here do not change if we adopt a different aging model, as in Sec.5.3 above).

The top panel in Fig. 15 shows the time evolution of electrons injected at the shock and downstream cooling. The integrated spectra corresponding to the entire B1 and within different 15" width stripes is shown in the middle panel. First, we notice that to a good approximation our reference model is able to reproduce the observed B1 spectrum over a wide frequency range, which makes our modeling of the downstream aging of the spectrum a good enough assumption for the sake of the following steps.

Secondly, to investigate the contamination of the B1 by the halo emission, we test a simple toy model scenario, in which we assume that the relic and the halo are not physically connected (hence their particle populations do not mix) but their emission is observed to be overlapping just in projection. We assume that the halo extends all the way up to the B1 region, at the same brightness that it is just below B1, and with an average spectral index. As a next step, we compute its contribution within each 15″ stripes (as shown by the grey line in Fig.15). This allows us to estimate the observable spectral curvature in the entire B1 region, by including both the radio components in an approximate way.

The resultant color-color plot for the different regions, using $\alpha^{650\,\rm MHz}_{150\,\rm MHz}$ and $\alpha^{3\,\rm GHz}_{1.5\,\rm GHz}$ is shown in the bottom panel of Fig. 15. Our observations and modeling give a similar trend in the color-color plane for the B1 region contamination by the halo. The concave regions in Fig. 14 and 15 seem indeed compatible with the superposition of the increasingly steeper spectrum from the older particles accelerated by shock at B1, and the power-law spectrum of the halo. It is important to emphasize here that in this simplistic model there is no ongoing particle acceleration as we go downstream of B1, because there is quite significant aging. On the other hand, we assume here a constant spectrum for the radio halo, on the basis that the energization of electrons may be happening in a very distributed and spatially uniform way (e.g. Brunetti et al. 2001; Brunetti & Jones 2014).

The concave curvature should, therefore, mark the frequency range (which decreases moving away from the B1 edge) at which the radio halo component dominates over the radio relic one, moving towards the center of 1RXS J0603.3+4214. According to this simple explanation there is no need to assume that turbulence (or in general, any process responsible for the appearance of the radio halo) is acting on fossil radio electrons injected by the shock responsible for the B1 relic, also because in this case the low energy particle would be accelerated first, and the spectrum would be flatter at low frequencies, and steeper at higher (e.g. Brunetti & Jones 2014, and references therein).

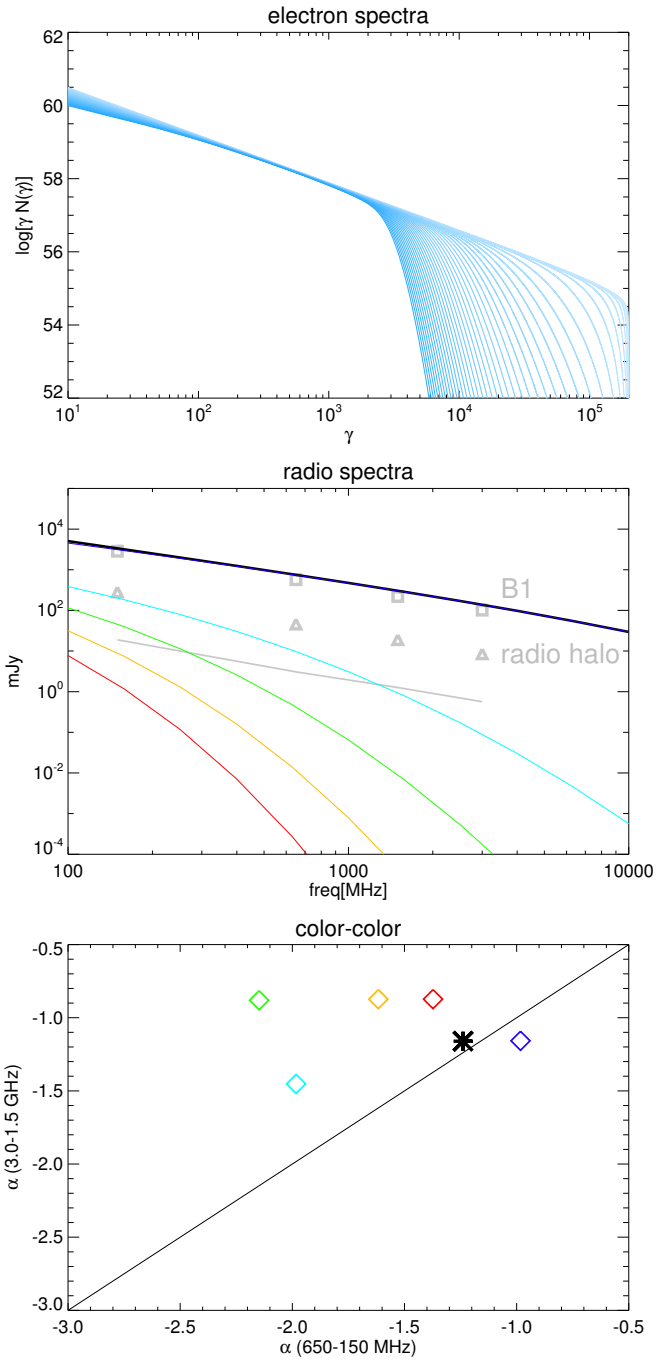


Fig. 15. Top panel: evolving spectrum of electrons accelerated by a $\mathcal{M} = 3.8$ shock and aging in a uniform 2.0 μG magnetic field (see text for other model parameters). Middle panel: evolving radio spectra as a function of time. The top black spectrum gives the integrated spectrum for the region corresponding to the entire B1 region, while the colored lines show the spectra within different 15″ ≈ 54 kpc thick stripes perpendicular to the shock propagation axis. The additional gray symbols show the observed total integrated spectrum for B1 (top squares) and the radio halo (lower tringles), while the gray line gives the estimated contribution from the radio halo within each single 15″ stripe (assuming a flat brightness distribution). Bottom panel: color-color plot obtained by comparing the $\alpha^{650\,\rm MHz}_{150\,\rm MHz}$ and $\alpha^{3\,\rm GHz}_{1.5\,\rm GHz}$ spectral slopes within the stripes with corresponding colors, as in the central panel.

Testing the hypothesis that the two emissions are related to physically disconnected acceleration regions is not easy, but in

principle it can be done by detecting polarized emission from the intermediate relic+halo region of 1RXS J0603.3+4214, and using Rotation Measure Synthesis (e.g. Brentjens & de Bruyn 2005) to detect a significant difference in Faraday depth of the two emitting structures. However, based on existing data (Rajpurohit et al., in prep.) no polarization is detected with available exposures in this region.

7. Conclusions and Summary

We presented results from deep, wide-band uGMRT (550-750 MHz) and VLA (2-8 GHz) radio observations of the galaxy cluster 1RXS J0603.3+4214. We focused on the diffuse extended radio sources in the cluster, namely the Toothbrush relic, fainter relics E and D, and a large extended radio halo which basically follows the X-ray surface brightness distribution of the ICM. These observations were combined with the existing VLA L-band (1-2 GHz) and LOFAR (120-180 MHz) data (van Weeren et al. 2016; Rajpurohit et al. 2018) in order to carry out a detailed radio continuum and spectral study of the cluster. From these observations, we have been able to characterize the integrated spectrum of the Toothbrush relic over an unprecedented frequency range. Here, we summarize our main findings:

1. Our new images confirm the existence of complex filamentary structures in the Toothbrush up to 8 GHz. We detect the other two fainter relics and the radio halo up to 4 GHz.

2. The radio integrated emission from the entire Toothbrush and subregions (B1, B2, and B3) closely follow a power-law, with an integrated spectral index of $\alpha = -1.16 \pm 0.02$. We do not find any evidence of spectral steepening of the relic emission at any frequency below 8 GHz.

3. The Toothbrush subregions B1, B2 and B3 show nearly identical spectra across a $\sim$ 2 Mpc scale, implying a very similar combination of shock properties across the shock front or the robust convergence of the spectral shape when averaged over some distribution of underlying properties.

4. Comparison with a recent numerical simulation of radio relics suggests that such a narrow variation in the integrated spectra are plausible when projection and cooling effects of electrons are properly taken into account. The simulation shows that there is a broad distribution of Mach number at the shock front, and that the ones at the high end dominate the spectral distribution. It seems plausible that the combination of the tail in the distribution towards high Mach numbers and the dependence of the radio luminosity on the Mach number determines the spectral index of the radio emission.

5. The spectral shapes inferred from spatially resolved regions reveal less homogeneity because the spectra show curvature. However, the observed steepening in these individual regions is still less than expected from any standard aging models. For individual filamentary structures we find differences in their spectral shapes, a direct indicator of the inhomogeneities.

6. The integrated spectra of portions of relics E and D show spectral shapes which are close to power laws, with different slopes at different locations. Other regions show some steepening at high frequencies. The types of inhomogeneities and/or physical conditions that would lead to this type of behavior are not yet clear.

7. In a simplistic model, we find that the downstream material emits an energy equivalent to about 1 % of the thermal energy due to synchrotron losses. This implies that the mechanism responsible for accelerating electrons to relativistic energies must be very efficient and that magnetic fields in the emitting volume below $\sim$ 1 µG are unlikely.

8. The integrated spectral index of the radio halo follows a well defined power law up to 3 GHz . A color-color analysis of regions within the radio halo shows no sign of spectral curvature.

9. Spectral analysis of the relic+halo region provides evidence that the two regions overlap along the line of sight. We present a simple model in which the observed positive curvature in the relic+halo spectra is well explained by the simple superposition, of an aging population of radio electrons injected by the relic shock, and of a different (physically disconnected) population of electrons in the radio halo.

Acknowledgements

K.R., F.V., and D.W. acknowledges financial support from the ERC Starting Grant "MAGCOW", no. 714196. Part of this work was performed at Thüringer Landessternwarte Tautenburg, Germany. The ENZO (http://enzo-project.org) simulation used in this work has been produced at the Jülich Supercomputing Centre (JFZ) under project HHH42 and *stressicm* (PI F.Vazza) as well as HHH44 (PI D. Wittor). Partial support for the work of L.R. is provided by U.S. National Science Foundation grant AST17-14205 to the University of Minnesota. A.D. acknowledges support by the BMBF Verbundforschung under the grant 05A17STA. We also acknowledge the usage of online storage tools kindly provided by the INAF Astronomical Archive (IA2) initiave (http://www.ia2.inaf.it).

The National Radio Astronomy Observatory is a facility of the National Science Foundation operated under cooperative agreement by Associated Universities. We thank the staff of the GMRT that made these observations possible. GMRT is run by the National Centre for Radio Astrophysics of the Tata Institute of Fundamental Research.

This paper is based (in part) on data obtained with the International LOFAR Telescope (ILT). LOFAR (van Haarlem et al. 2013) is the Low Frequency Array designed and constructed by ASTRON. It has facilities in several countries that are owned by various parties (each with their own funding sources), and that are collectively operated by the ILT foundation under a joint scientific policy.

References

Baars, J. W. M., Genzel, R., Pauliny-Toth, I. I. K., & Witzel, A. 1977, A&A, 61, 99
Basu, K., Vazza, F., Erler, J., & Sommer, M. 2016, A&A, 591, A142
Battaglia, N., Pfrommer, C., Sievers, J. L., Bond, J. R., & Enßlin, T. A. 2009, MNRAS, 393, 1073
Blandford, R. & Eichler, D. 1987, Phys. Rep., 154, 1
Bonafede, A., Brüggen, M., van Weeren, R., et al. 2012a, MNRAS, 426, 40
Bonafede, A., Brüggen, M., van Weeren, R., et al. 2012b, MNRAS, 426, 40
Bonafede, A., Giovannini, G., Feretti, L., Govoni, F., & Murgia, M. 2009, A&A, 494, 429
Botteon, A., Brunetti, G., Ryu, D., & Roh, S. 2019, arXiv e-prints, arXiv:1907.00966

Botteon, A., Gastaldello, F., Brunetti, G., & Kale, R. 2016, MNRAS, 463, 1534
Brentjens, M. A. & de Bruyn, A. G. 2005, A&A, 441, 1217
Brown, S. & Rudnick, L. 2011, MNRAS, 412, 2
Brüggen, M., van Weeren, R. J., & Röttgering, H. J. A. 2012, MNRAS, 425, L76
Brunetti, G., Blasi, P., Cassano, R., & Gabici, S. 2004, MNRAS, 350, 1174
Brunetti, G. & Jones, T. W. 2014, International Journal of Modern Physics D, 23, 1430007
Brunetti, G., Rudnick, L., Cassano, R., et al. 2013, A&A, 558, A52
Brunetti, G., Setti, G., Feretti, L., & Giovannini, G. 2001, MNRAS, 320, 365
Bykov, A. M., Vazza, F., Kropotina, J. A., Levenfish, K. P., & Paerels, F. B. S. 2019, Space Sci. Rev., 215, 14
Chandra, P., Ray, A., & Bhatnagar, S. 2004, ApJ, 612, 974
Chang, J. S. & Cooper, G. 1970, Journal of Computational Physics, 6, 1
Cornwell, T. J., Golap, K., & Bhatnagar, S. 2008, IEEE Journal of Selected Topics in Signal Processing, 2, 647
Di Gennaro, G., van Weeren, R. J., Andrade-Santos, F., et al. 2019, ApJ, 873, 64
Di Gennaro, G., van Weeren, R. J., Hoeft, M., et al. 2018, ApJ, 865, 24
Domínguez-Fernández, P., Vazza, F., Brüggen, M., & Brunetti, G. 2019, MNRAS, 486, 623
Donnert, J. & Brunetti, G. 2014, MNRAS, 443, 3564
Donnert, J., Vazza, F., Brüggen, M., & ZuHone, J. 2018, ArXiv e-prints [arXiv:1810.09783]
Enßlin, T. A. 2002, A&A, 396, L17
Ensslin, T. A., Biermann, P. L., Klein, U., & Kohle, S. 1998, A&A, 332, 395
Feretti, L., Giovannini, G., Govoni, F., & Murgia, M. 2012, A&A Rev., 20, 54
Ginzburg, V. L. & Syrovatskii, S. I. 1965, ARA&A, 3, 297
Ha, J.-H., Ryu, D., & Kang, H. 2018, ApJ, 857, 26
Hoang, D. N., Shimwell, T. W., Stroe, A., et al. 2017, ArXiv e-prints [arXiv:1706.09903]
Hoeft, M. & Brüggen, M. 2007, MNRAS, 375, 77
Hoeft, M., Brüggen, M., Yepes, G., Gottlöber, S., & Schwope, A. 2008, MNRAS, 391, 1511
Hoeft, M., Nuza, S. E., Gottlöber, S., et al. 2011, Journal of Astrophysics and Astronomy, 32, 509
Itahana, M., Takizawa, M., Akamatsu, H., et al. 2015, PASJ, 67, 113
Itahana, M., Takizawa, M., Akamatsu, H., et al. 2017, PASJ, 69, 88
Jaffe, W. J. & Perola, G. C. 1973, A&A, 26, 423
Kale, R., Dwarakanath, K. S., Bagchi, J., & Paul, S. 2012, MNRAS, 426, 1204
Kang, H. & Ryu, D. 2016, ApJ, 823, 13
Kang, H., Ryu, D., & Jones, T. W. 2012, ApJ, 756, 97
Kardashev, N. S. 1962, Soviet Ast., 6, 317
Katz-Stone, D. M., Rudnick, L., & Anderson, M. C. 1993, ApJ, 407, 549
Kierdorf, M., Beck, R., Hoeft, M., et al. 2017, A&A, 600, A18
Komissarov, S. S. & Gubanov, A. G. 1994, A&A, 285, 27
Liang, H., Hunstead, R. W., Birkinshaw, M., & Andreani, P. 2000, ApJ, 544, 686
Loi, F., Murgia, M., Govoni, F., et al. 2017, MNRAS, 472, 3605
Malu, S., Datta, A., & Sandhu, P. 2016, Ap&SS, 361, 255
Markevitch, M., Govoni, F., Brunetti, G., & Jerius, D. 2005, ApJ, 627, 733
McMullin, J. P., Waters, B., Schiebel, D., Young, W., & Golap, K. 2007, in Astronomical Society of the Pacific Conference Series, Vol. 376, Astronomical Data Analysis Software and Systems XVI, ed. R. A. Shaw, F. Hill, & D. J. Bell, 127
Mohan, N. & Rafferty, D. 2015, PyBDSM: Python Blob Detection and Source Measurement, Astrophysics Source Code Library
Nuza, S. E., Gelszinnis, J., Hoeft, M., & Yepes, G. 2017, MNRAS, 470, 240
Offringa, A. R., de Bruyn, A. G., Biehl, M., et al. 2010, MNRAS, 405, 155
Ogrean, G. A., Brüggen, M., van Weeren, R. J., et al. 2013, MNRAS, 433, 812
Owen, F. N., Rudnick, L., Eilek, J., et al. 2014, ApJ, 794, 24
Pacholczyk, A. G. 1970, Radio astrophysics. Nonthermal processes in galactic and extragalactic sources
Perley, R. A. & Butler, B. J. 2013, ApJS, 204, 19
Petrosian, V. 2001, ApJ, 557, 560
Pinzke, A., Oh, S. P., & Pfrommer, C. 2013, MNRAS, 435, 1061
Rajpurohit, K., Hoeft, M., van Weeren, R. J., et al. 2018, ApJ, 852, 65
Rau, U. & Cornwell, T. J. 2011, A&A, 532, A71
Rudnick, L., Katz-Stone, D. M., & Anderson, M. C. 1994, ApJS, 90, 955
Rybicky, G., Lightman, A. P., & Domke, H. 1982, Astronomische Nachrichten, 303, 142
Sarazin, C. L. 1999, ApJ, 520, 529
Sarazin, C. L., Finoguenov, A., & Wik, D. R. 2013, Astronomische Nachrichten, 334, 346
Shimwell, T. W., Brown, S., Feain, I. J., et al. 2014, MNRAS, 440, 2901
Shimwell, T. W., Markevitch, M., Brown, S., et al. 2015, MNRAS, 449, 1486
Skillman, S. W., Hallman, E. J., O'Shea, B. W., et al. 2011, ApJ, 735, 96
Skillman, S. W., Xu, H., Hallman, E. J., et al. 2013, ApJ, 765, 21
Stroe, A., Rumsey, C., Harwood, J. J., et al. 2014, MNRAS, 441, L41
Stroe, A., Shimwell, T., Rumsey, C., et al. 2016, MNRAS, 455, 2402
Stroe, A., van Weeren, R. J., Intema, H. T., et al. 2013, A&A, 555, A110
Stuardi, C., Bonafede, A., Wittor, D., et al. 2019, arXiv e-prints, arXiv:1908.11868
Thierbach, M., Klein, U., & Wielebinski, R. 2003, A&A, 397, 53
Thölken, S., Reiprich, T. H., Sommer, M. W., & Ota, N. 2018, A&A, 619, A68
Trasatti, M., Akamatsu, H., Lovisari, L., et al. 2015, A&A, 575, A45
van Weeren, R. J., Andrade-Santos, F., Dawson, W. A., et al. 2017a, Nature Astronomy, 1, 0005
van Weeren, R. J., Brüggen, M., Röttgering, H. J. A., et al. 2011, A&A, 533, A35
van Weeren, R. J., Brunetti, G., Brüggen, M., et al. 2016, ApJ, 818, 204
van Weeren, R. J., de Gasperin, F., Akamatsu, H., et al. 2019, Space Sci. Rev., 215, 16
van Weeren, R. J., Ogrean, G. A., Jones, C., et al. 2017b, ArXiv e-prints [arXiv:1701.04096]
van Weeren, R. J., Röttgering, H. J. A., Intema, H. T., et al. 2012, A&A, 546, A124
Vazza, F. & Brüggen, M. 2014, MNRAS, 437, 2291
Vazza, F., Eckert, D., Brüggen, M., & Huber, B. 2015, MNRAS, 451, 2198
Wittor, D., Hoeft, M., Vazza, F., Brüggen, M., & Domínguez-Fernández, P. 2019, MNRAS, 490, 3987
Wittor, D., Vazza, F., & Brüggen, M. 2017, MNRAS, 464, 4448